

Contents — A through D

Multiple Impacts Across the Cretaceous-Tertiary Boundary <i>T. Adatte, G. Keller, W. Stinnesbeck, M. Harting, D. Stüben, and U. Kramar</i>	4048
Large Meteorite Impact on Sediments: Where Does the Lime Go? <i>P. Agrinier and I. Martinez</i>	4042
Distal Ejecta from the Ries Crater — Moldavites and Projectile <i>N. A. Artemieva</i>	4050
Interaction of the Ejecta Plume and the Atmosphere During the Deposition of the Uppermost Suevite Layers at the YAX-1 Drilling Site, Chicxulub, Mexico <i>N. A. Artemieva, D. Stöffler, L. Hecht, R. T. Schmitt, and R. Tagle</i>	4063
A New View of Martian Impact Craters <i>N. G. Barlow</i>	4018
Effects of Pre-Existing Target Structure on the Formation of Large Craters <i>O. S. Barnouin-Jha, M. J. Cintala, and D. A. Crawford</i>	4106
The Impact Rate of Small Asteroids at the Earth's Surface <i>P. A. Bland and N. A. Artemieva</i>	4047
The Eastern Hudson Bay Arc, Canada: Part of a Multi-Ringed Basin <i>M. E. Brookfield</i>	4010
Effect of the Supposed Giant Impact Crater on the Geologic Evolution of the Ural Mountain Range <i>G. A. Burba</i>	4117
Geochemistry of Accretionary Lapilli from a Cretaceous-Tertiary Impact Breccia, Guayal, Mexico <i>E. Burns, H. Sigurdsson, S. Carey, and S. D'Hondt</i>	4113
Numerical Simulations of Silverpit Crater Collapse <i>G. S. Collins, B. A. Ivanov, E. P. Turtle, and H. J. Melosh</i>	4126
Mesoscale Computational Investigation of Shocked Heterogeneous Materials with Application to Large Impact Craters <i>D. A. Crawford, O. S. Barnouin-Jha, and M. J. Cintala</i>	4119
A Model of Early Condensate Composition in Impacts <i>D. de Niem</i>	4069
On the Shock Behavior of Anhydrite and Carbonates — Is Post-Shock Melting the Most Important Effect? Examples from Chicxulub <i>A. Deutsch, F. Langenhorst, U. Hornemann, and B. A. Ivanov</i>	4080
Synthesis of Nanocrystalline Diamond and 6H Diamond Polytype <i>N. Dubrovinskaia, L. Dubrovinsky, and F. Langenhorst</i>	4065
Phase Relations in TiO ₂ at Elevated Pressures and Temperatures <i>L. Dubrovinsky and N. Dubrovinskaia</i>	4060

MULTIPLE IMPACTS ACROSS THE CRETACEOUS–TERTIARY BOUNDARY. T. Adatte¹, G. Keller², W. Stinnesbeck³, M. Harting⁴, D. Stüben⁴, Kramar U.⁴, ¹Geological Institute, University of Neuchâtel, Neuchâtel, CH-2007, Switzerland, thierry.adatte@unine.ch ²Department of Geosciences, Princeton University, Princeton 08544, USA; ³Geologisches Institut, Universität Karlsruhe, 76128 Karlsruhe, Germany; ⁴Institut für Mineralogie und Geochemie, Universität Karlsruhe, 76128 Karlsruhe, Germany

Spherules in sediments across the Cretaceous–Tertiary (K/T) transition in Central America and the Caribbean are commonly interpreted as ejecta from the Chicxulub impact on Yucatan. Their stratigraphic ages, however, are variable spanning from the late Maastrichtian to the early Danian.



Figure 1. Locations of spherule-bearing K/T boundary sections in Central America, and the Caribbean.

In northeastern Mexico, three and sometimes four spherule-rich layers are interbedded with marls of the Mendez Formation that span the last 300 kyr of the Maastrichtian (*Plummerita hantkeninoides*, CF1 zone). [1]. In Guatemala [2], Belize and Haiti [3], spherule-rich deposits are interbedded with early Danian sediments of the *Parvularugoglobigerina eugubina* (Pla) zone. ODP Sites 1001 and 1049 are very condensed and incomplete, and therefore provide no evidence of deposition precisely at the K/T boundary [4]. Smectites analyzed from spherule-rich deposits are very similar and indicate a common origin, except for those in northeastern Mexico, which are compositionally different mainly due to dilution by terrigenous influx related to tectonic activity in the nearby Sierra Madre Oriental [5]. The presence of almost pure Mg-smectite (Cheto type) in spheroid beds and diamictite at Albion Island and Armenia of northern and central Belize and in microspherule deposits of southern Belize and eastern Guatemala [6] indicate therefore a common glass source for both types of spherule deposits and links these to the Chicxulub impact. In addition to the pre-K/T spherule deposits and the well known K/T boundary Ir anomaly and impact event, there is also a wide-

spread early Danian *P. eugubina* subzone Pla(l) Ir anomaly of cosmic origin.

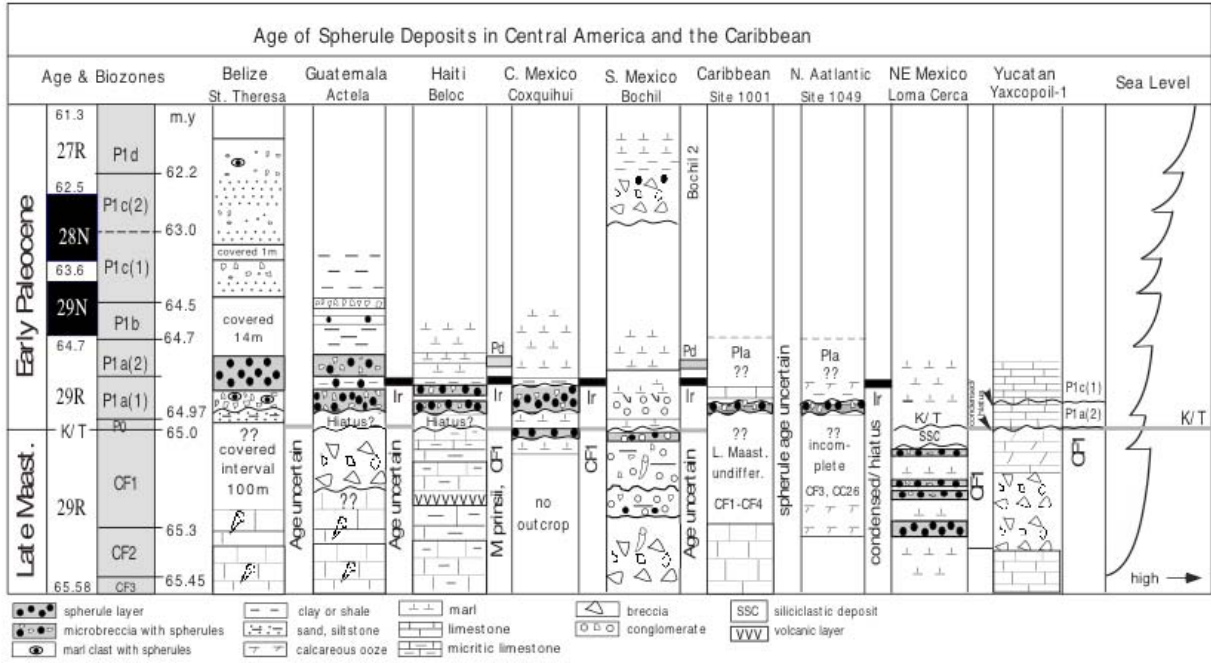
Multiple impacts (comet shower?) are most consistent with current evidence of spherules, Ir anomalies and climate change during the late Maastrichtian to early Danian and support three impact events. The first impact, marked by the oldest spherule deposit in NE Mexico, is related to the Chicxulub crater as suggested by our recent results from the new core Yaxcopoil-1. This event occurred in the late Maastrichtian at about 65.3 Ma nearly coincident with major Deccan volcanism and rapid global warming between 65.4–65.2 Ma [7, 8]. Subsequent late Maastrichtian and early Danian spherule layers may have been repeatedly reworked and redeposited from this event by currents and tectonic activity, though an additional spherule-producing event cannot be completely ruled out.

The second impact is the well-known K/T boundary event marked worldwide by an Ir anomaly and other cosmic signals, though this event is not well represented in the Caribbean and Central America due to erosion as a result of current and tectonic activity. The third impact occurred in the early Danian *P. eugubina* subzone Pla(l) about 100 kyr after the K/T boundary and is marked by a widespread Ir anomaly in the Caribbean and Central America.

The end of the Cretaceous experienced therefore multiple impacts (e.g. comet shower), rather than a single large impact as generally hypothesized. Chicxulub was one of these with a crater size of about 80–120 km in diameter. Other smaller late Maastrichtian craters have recently been reported from the Ukraine (Boltys crater 65.2±0.6 Ma, [9]) and the Silverpit crater in the North Sea [10]. In addition, late Maastrichtian Ir and PGE anomalies have been reported from Oman [11] and from Israel with an age of lower zone CF1 [12].

- [1] Stinnesbeck et al. (2001) *Canadian Journal of Earth Sciences* 38, 229–238. [2] Stinnesbeck et al. (1997) *Geologische Rundschau*, 86, 686–709. [3] Keller et al. (2001) *Canadian Journal of Earth Sciences* 38, 197–227. [4] Keller G. et al. (2003) *Earth-Science Reviews* 1283, 1–37. [5] Adatte et al. (1996) *Geol. Soc. Am. Special Paper* 307, 197–210. [6] Keller et al., (2003) *Geological Society of London*, in press. [7] Hoffman C. et al. (2000) *EPSL* 180, 13–27. [8] Li L. and Keller G. (1998) *Geology* 26, 995–998. [9] Kelley

P.S. and Gurov E. (2002), *Met. & Plan. Sci.* 37, 1031-1043. [10] Stewart S.A. and Allen P.J. (2002, *Nature* 418, 520-522. [11] Ellwood B.B. et al. (2003) *EPSL* 206, 529-540. [12] Adatte T. et al. in prep.



LARGE METEORITE IMPACT ON SEDIMENTS : WHERE DOES THE LIME GO ? Pierre Agrinier and Isabelle Martinez both at IPG Paris, 4 place Jussieu, 75252 Paris Cedex 05 France (agrinier@ipgp.jussieu.fr; martinez@ipgp.jussieu.fr; Phone 33 1 44 27 28 11, fax 33 1 44 27 28 30)

Shock metamorphism induced by large meteorite impacts on Earth decomposes sediments (carbonates : CaCO_3 and sulfates : CaSO_4) into CaO , CO_2 and SO_2 . For the Chicxulub case at the K/T boundary, up to 816 Gigatons of CO_2 and up to 214 Gigatons of SO_2 were liberated into the atmosphere [1], [2] & [3]. Though numerous works have depicted the resulting environmental consequences of dispersing CO_2 , SO_2 , dust into the atmosphere (greenhouse warming, aerosol cooling, acid rains, ...), no study have yet described the fate of the corresponding formed CaO (up to 1040 Gtons). Using the lowest published numbers, the Chicxulub impact liberated at least 401 Gtons.

Assuming that CaO can rapidly (within less than 1000 seconds) backreacts with CO_2 and SO_2 at moderate temperature (500 to 1000 K) to form secondary carbonates and sulfates [4] & [5], up to 50 % of the initially released CaO , CO_2 and SO_2 are backreacted. This CaO sink leave at least 200 Gt of unreacted CaO cooled in the impact-expanding cloud and deposited with impact dust over the Earth surface ($5 \cdot 10^{18} \text{ cm}^2$). It represents a mean contribution of 40 mg of CaO per square centimeter.

Considering the reactivity of CaO (lime) and of its hydrated product (Ca(OH)_2 ; portlandite) at low temperature for a short period of time (days-month). This would produce harmful environmental effects (organic matter is destroyed, natural waters are strongly depleted in carbonates and metals [6], [7], [8] & [9] and symptomatic isotopic ^{13}C - and ^{18}O -depleted carbonates [10].

Neutralization by fast atmospheric CO_2 pumping and acid rains (H_2CO_3 , H_2SO_4) produced by the impact liberated- CO_2 and SO_2 would control the duration of this high pH effect on lands, while at the surface of the oceans, additional mixing with normal pH (8.2) deep seawater would further reduce the duration of this high pH effect.

The high reactivity of lime would control the lifetime of the K/T meteorite impact atmospheric CO_2 and SO_2 perturbations to a very short time scale, probably much less than one year.

References: [1] Gupta S.C, Love S.G and Ahrens T.J., 2002 : Earth Planet. Sci. Lett., 201, 1-12. [2] Ivanov B.A., Badukov D.D., Yakovlev O.I., Gerasimov M.V., Dikov Y.P., Pope K.O. and Ocampo A.C., 1996, , in : The Cretaceous Tertiary event and other catastrophes in Earth history, Ryder G.,

Fortovsky and Gartner S. (eds). Geol. Soc. Amer. Spec. Pap., 307, 125-142. [3] Pierazzo E., Kring D.A. and Melosh H.J., 1998, J. Geophys. Res., Planet 103(E12), 28607-28625. [4] Martinez I., Agrinier P., Schärer U. and Javoy M., 1994, Earth Planet. Sci. Lett., 121, 559-574. [5] Agrinier P., Deutsch A., Schärer U. and Martinez I., 2001, Geochim. Cosmochim. Acta, 65, 2615-2632. [6]. Chambers P.A., Prepas E.E., Ferguson M.E., Serediak M., Guy M. and Holst M., 2001, Freshwater Biology, 46-8, 1121-1130. [7] Robertson L.J., Campbell A.T. and Smith H.V., 1992, Appl. & Environm. Microbiol. 58 (11), 3494-3500. [8] Holliday, S. L., Scouter, A. J., and Bechat, L. R., 2001, J. Food Protection, 64, (10). pp. 1489 – 1495. 733. [9] Mignotte-Cadiergues B., Maul A., Huyard A., Capizzi S. and Schwartzbrod L., 2001, Water Science & Technology 43, 195-200. [10] Usdowski E. and Hoefs J., 1986, Earth Planetary Sci. Lett., 80, 130-134.

DISTAL EJECTA FROM THE RIES CRATER – MOLDAVITES AND PROJECTILE. N. A. Artemieva. Institute for Dynamics of Geospheres, Russian Academy of Science, Leninsky pr., 38, bldg.1, 119334, Moscow, Russia, nata_art@mtu-net.ru

Introduction: Using detailed geological, petrographic, geochemical, and geographical constraints we have performed numerical modeling studies that relate the Steinheim crater ($D_a = 3.8$ km), the Ries crater ($D_a = 24$ km) in Southern Germany, and the moldavite (tektite) strewn field. The known moldavite strewn field extends from about 200 to 450 km from the center of the Ries to the ENE forming a fan with an angle of about 57° . An oblique impact of a binary asteroid from a WSW direction appears to explain the locations of the craters and the formation and distribution of the moldavites [1]. In a presented study we attempt to answer more questions concerning this particular strewn field as well as other questions common for all tektites. What is the maximum “numerical” size of the moldavite strewn field? How is this size connected with the crater size and the impact conditions? How many tektites may be found theoretically without weathering and surface erosion? What is the size of tektites? Why they are not contaminated by projectile? Where is the projectile material?

Hydrocode and EOS in use. Impact simulations were carried out with the three-dimensional (3D) hydrocode SOVA [3] coupled to a tabular version of the ANEOS equation of state package [4]. The code allows to describe particle motion in the evolving ejecta-gas plume, including the interaction of particles with the gas. Details of numerical model and geological input may be found in [1,2].

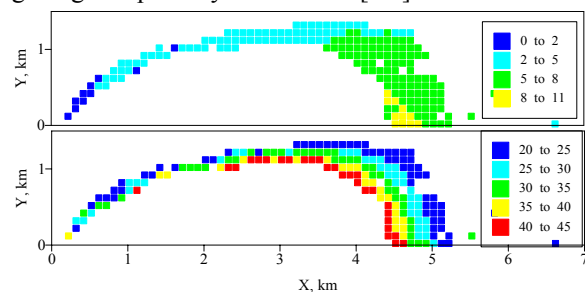


Fig.1. Initial position of tektite melt at the target surface (only half space with $y > 0$) is shown. The projectile with diameter of 1.5 km strikes from the left at the point (0,0). Upper plate shows ejection velocity in km/s, bottom plate is for maximum compression in GPa.

Excavation depth and chemistry. Moldavites originate from the upper 40 m of sandy layer, presented in the numerical model and underlain by thick layer of limestone. In reality it is not a

continuous unit, but, probably, some chaotic spots with various thickness. In this upper layer shock pressure drops quickly with a distance and at 5 km from the impact point is below melting pressure for a porous quartz (45 GPa). Figure 1 shows surface material, molten after an impact - possible tektites. It is totally within the growing crater (the Ries final diameter is 26 km). Ejection velocity varies from 1-2 km/s behind the projectile to 8-11 km/s in a downrange direction.

The model with more thick sandy layer reveals that 70% of all tektites originate from the upper 20 m, 90% - from the upper 40 m, and only 10% of the material is initially below this depth. The results correlate with ^{10}Be composition of tektites [5].

Tektites size and shape. The size and shape of individual particles are influenced by many processes (strain rates, surface tension, the ratio between melt and vapor) with poorly known parameters [6]. In our simplified approach, material disruption occurs when the density of the solid or molten material drops below the normal density - the material is subject to tension. The diameter of molten particles is in the range of 1-3 cm, corresponding to the average size of tektites [5,7]. Particle size drops to 0.01 cm if particles are produced from a two-phase mixture, where vapor and melt coexist (microtektites)

Mixing with projectile. The meteoritical component in tektites is very low, if any [5]. This fact is widely used against an impact fusion hypothesis of tektites origin [8]. On the basis of numerical model we may suggest that two types of melts (projectile and upper target) have no enough time for mixing, as both are ejected from the growing crater very early, during the first seconds after an impact (**Fig.2**). Diffusion in a liquid, as well as the turbulent mixing, demands much longer time interval. Only gas diffusion may be important, but in our model tektites are produced from the pure melt with minor vapor content. Independent confirmation of no-mixing in moldavites is their chemical composition - a mixture of precursor sedimentary rocks (clay, sand, limestone) prior the impact event [9]. Nevertheless, tektites and molten projectile material are ejected with similar velocities and move along similar trajectories. It means that they will be deposited not far from each other. Thus, the question arises - is it possible to find “tektites” of extraterrestrial origin?

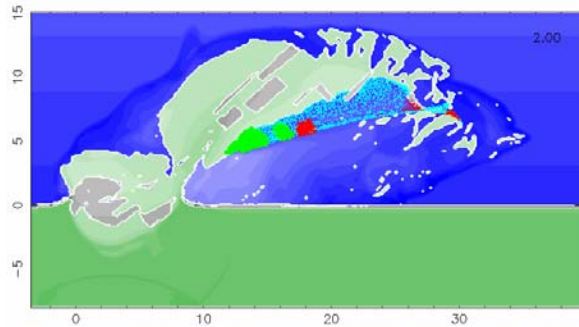


Fig 2. Ejecta in the plane of symmetry 2 seconds after the 30-degree impact for the Ries crater. The projectile strikes the surface at the point (0,0). Red particles are tektites, green ones – solid target ejecta, blue particles correspond to projectile material (part of the projectile is still a vapor).

Size and shape of the strewn field. For 30°, 20 km/s impact total melt production from the upper layer is ~700 Mt [1]. Practically all the melt is ejected and disrupted into the particles – 150 Mt of tektites and 510 Mt of microtektites. The total time from tektites ejection to their deposition as a strewn field varies from 10 minutes to hours. The temperature of the entraining gas is high, the particles do not cool quickly, having enough time to be aerodynamically shaped and to lose volatiles. Some of the particles reach an altitude above 1000 km and their deposition is influenced by the Earth's rotation and local weather conditions. Neglecting those processes we receive huge strewn field even for the Ries crater. All tektites and 80% of microtektites are deposited and the resulting strewn field stretches 6000 km along the projectile trajectory and 4000 km in the perpendicular direction (**Fig. 3**, upper plate). The shape of this strewn field differs substantially from the known moldavite strewn field (and is an order of magnitude larger), but its trefoil strongly resembles the youngest Australia-Asian strewn field.

Molten projectile is deposited similarly with higher area density, but the size projectile particles is much smaller than tektites (projectile has higher compression and higher temperature in average). The role of asteroid composition, which is different from granite, is not clear yet. These particles degrade much quicker in terrestrial environment than tektites and may be found only within a young strewn field. The soil near tektites may be contaminated by the extraterrestrial material – the problem should be investigated in a future more carefully in collaboration with geochemists.

Impact angle strongly influences final strewn field size and tektites' concentration. In the case of an oblique impact of 15°, the projectile distribution is similar, while tektites strewn field is much smaller.

Concentration of tektites in the vicinity of the crater is an order of magnitude higher (**Fig.4**).

Acknowledgments. The study is supported by NASA PGG grant and Russian Foundation of Basic Researches grant 01-05-64564-a

References: [1] Stoffler D. et al. (2002) *M&PS* 37, 1893-1908. [2] Artemieva N. et al. (2002) *Bulletin of the Czech Geological Survey* 77, 303-311. [3] Shuvalov V. (1999) *Shock Waves* 9, 381-390. [4] Thompson S. L. and Lauson H. S. (1972) *SC-RR-61 0714*, 119 p [5] Montanari A, Koeberl C (2000) *Lecture Notes in Earth Sciences* 93, 364 p. [6] Melosh H. J. and Vickery A. (1991) *Nature* 350, 494-497. [7] O'Keefe J. A. (1963) *Tektites*. 228 p. [8] O'Keefe J. A. (1994) *Meteoritics* 29, 73-78. [9] Meisel T. et al. *M&PS* 32, 493-502.

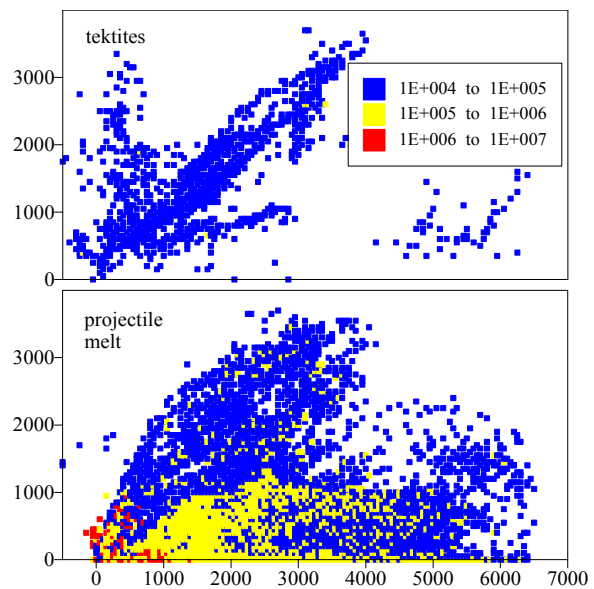


Fig. 3. Half of the strewn field ($y > 0$) for 30-degree, 20 km/s impact into the Ries target. Mass of tektites (upper plate) and projectile melt (bottom plate) per square km, averaged over the area 50km×50km, is shown (10^6 kg/km² means 1 kg of tektites per m², or 30 tektites with average size of 3 cm).

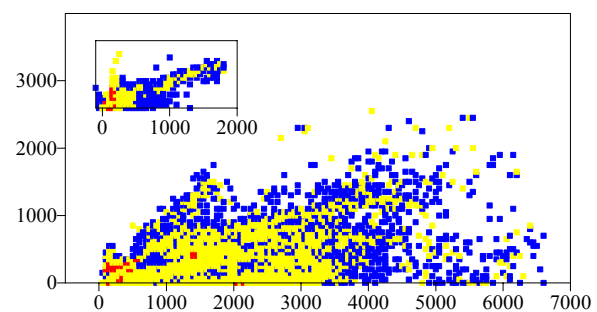


Fig. 4. The same as Fig. 3 for lower impact angle of 15°. Tektites distribution is shown in the left upper corner.

INTERACTION OF THE EJECTA PLUME AND THE ATMOSPHERE DURING THE DEPOSITION OF THE UPPERMOST SUEVITE LAYERS AT THE YAX-1 DRILLING SITE, CHICXULUB, MEXICO.

N. A. Artemieva¹, D. Stöffler², L. Hecht², R. T. Schmitt², and R. Tagle². ¹Institute for Dynamics of Geospheres, Leninsky pr., 38, Bldg.1, 119334, Moscow, Russia, nata_art@mtu-net.ru. ²Institute für Mineralogie, Museum Naturkunde, Humboldt University, Invalidenstrasse 43, 10099 Berlin, Germany, dieter.stoeffler@rz.hu-berlin.de

Introduction. The ICDP drilling Yaxcopoil-1, located in the annular ring trough of the 190 km Chicxulub peak ring impact basin, exposes some 100 m of polymict, melt-rich suevitic breccias below 795 m of post-impact Tertiary sediments. The suevitic breccia section has a layered structure in which 6 units can be defined [1, 2]. The upper two units, some 29 m thick, display a very unusual fine grain size and a distinct grain size sorting which is distinctly different from the underlying suevitic layers and is unknown from any other large impact crater at a corresponding geologic position, e. g. the Ries crater [3]. We use 3D numerical modeling of the impact event to reproduce interaction of vapor plume, solid and molten ejecta, atmosphere and to estimate the time-scale and atmospheric conditions for suevite deposition.

Stratigraphy, classification, and origin of various suevite-type layers. The 100m thick sequence of polymict allochthonous suevite-type breccias is interpreted to represent three major stratigraphic subunits which are formed by distinctly different processes [2]: Units 5 and 6 were produced by ground surging of polymict material during transient cavity formation and by lateral highly dynamic transport of mainly coherent melt rock material during cavity and central uplift collapse [4], units 3 and 4 by fallback of polymict material from the ejecta plume, and units 1 and 2 (sorted suevite) by late fall back of polymict material from the upper ejecta plume through the restored atmosphere. This latter hypothesis is tested in this contribution in more detail.

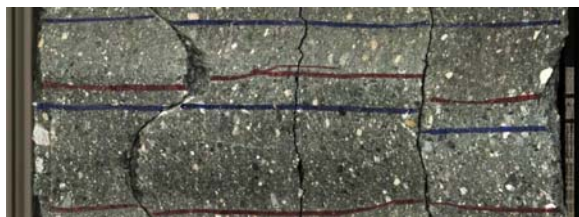


Fig.1. Upper sorted suevite from YAX-1 (794.63 – 807.75 m).

Characteristics of the sorted suevite. The 2 units of this suevite have a limited variation of grain size which ranges from about 4 cm (Upper suevite – Fig. 1), with most clasts < 5 mm, and from about 9 cm (Lower suevite.), with most clasts < 1- 2 cm, to less than 100 μ m. The components are dominated by two texturally and chemically different types of silicate melt particles, abundant clasts from the crystalline

basement and limestone clasts from the pre-impact sedimentary rock sequence. The matrix consists of calcite grains and tiny, crystallized melt particles and is interpreted to be primarily of clastic origin. Except for the ~ 50 cm thick transition zone to the post-impact Tertiary carbonate sediments, no distinct bedding or graded bedding or layering has been observed in the whole unit of sorted suevite.

Atmospheric versus aquatic sorting processes. The described properties of the sorted suevite, particularly the lack of any type of bedding or layering appears not to be compatible with an aquatic sedimentary environment during the deposition of the suevite material. The secondary calcite observed in the suevite matrix is more readily explained by hydrothermal post-depositional activity [5] rather than by precipitation of calcite from oceanic water. The general tendency of a decreasing grain size from bottom (unit 2) to top (unit 1) speaks in favor of a settling particles through the atmosphere.

Numerical model. Our impact simulations were carried out with the three-dimensional (3D) hydrocode SOVA [6] coupled to ANEOS-derived [7] equation of state tables for the materials used in the simulations. A feature that makes SOVA unique among hydrocodes used for impact cratering studies is the implementation of a procedure to describe particle motion in the evolving ejecta-gas plume, including the interaction of particles with the gas.

The target layout has been reconstructed and simplified from the known pre-impact stratigraphy [8]. It consists of a 3 km thick sedimentary layer (calcite EOS); the 30-km-thick crystalline basement below the sedimentary layer (non-porous granite with the EOS from [9]) is underlain by dunite mantle. The 12-km in diameter projectile (granite EOS) strikes the surface with the impact velocity of 20 km/s and various impact angles from 30° to 90°.

Modeling of the sorting process. First we make simplified estimates of a settling time for the particles of different sizes, assuming interaction of those particles with undisturbed atmosphere. The particles are subject to gravity and Stokes drag, which is particularly important for low velocity small particles and the drag in high-velocity flow. Initially those particles are carried to high altitudes by the vapor plume. The estimates may be considered as the lower limit of the settling time, as the remnant turbulence in

atmosphere as well as higher initial position prolong the process.

From Fig.2 it is clear that particles larger than 1 cm settle during the first 10 minutes. This time interval is comparable with the time of crater formation [4]. Most probably, those particles are strongly influenced by the cratering process, ground surge, atmospheric flow, etc. In this case our simplified estimates are not correct and a full-scale modeling of ejection and plume-particle interaction would be needed. But smaller, mm-sized particles, typical for the Upper suevite, precipitate during 1-2 hours after the crater and plume collapse and may create well-layered deposits sorted by atmosphere.

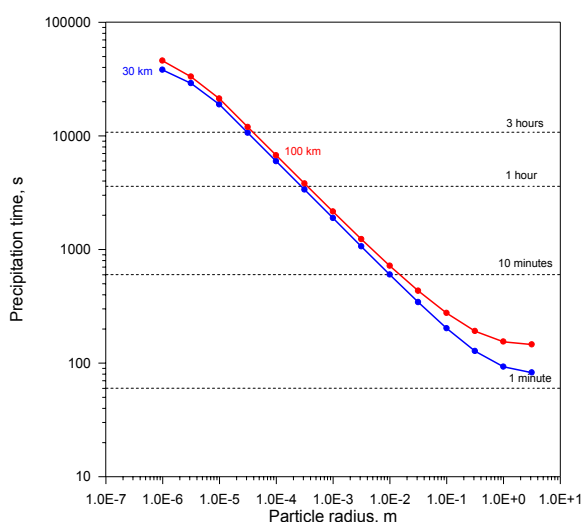


Fig 2. Settling time for the particles of various sizes from an altitude of 30 km (blue curve) and 100 km (red curve) through undisturbed atmosphere.

Interaction of vapor plume with ejecta. Vapor plume arises immediately after an impact and consists of the projectile and sedimentary layer material. Both are two-phase mixtures with the temperatures of ~ 3000 K and 1000 K, respectively (Fig. 3). Approximately ten seconds after an impact molten and shock-compressed solid material of the basement is entrained into the plume with initial velocity of 0.2 – 2 km/s. The degree of shock compression varies from a few GPa (solid shock-modified granite) to 200 GPa (molten material with minor content of vapor).

Later we decoupled the process of crater growth and plume rising in order to model ejecta plume at high altitudes as it is impossible to describe both processes at the same run with proper accuracy.

Projectile fate. The most part of the projectile leaves the growing crater during a few seconds with the velocity of 4 (45° impact) – 10 km/s (30°). The projectile material (granite in this model) is totally melted and partially vaporized. A lot of vapor from

sedimentary layer disrupts projectile material in billions of tiny particles. This may explain our findings that the platinum group elements in the suevite units lack any projectile signature [9]

Time scales. Transient crater reaches the maximum volume within the first minute while crater collapse continues the next 10 minutes [4]. Vapor plume (in reality – mixture of vapor, two-phase mixture and solid particles) occupies a huge area and allows world-wide distribution of the material ejected at the early stage of an impact. Ejecta deposition within the crater (fall back material) prolongs hours after an impact for fine-grained particles.

Conclusion. Comparison of numerical modeling with YAX-1 core data shows that upper suevite layer is the result of early ejecta deposition through atmosphere with minor influence of vapor plume.

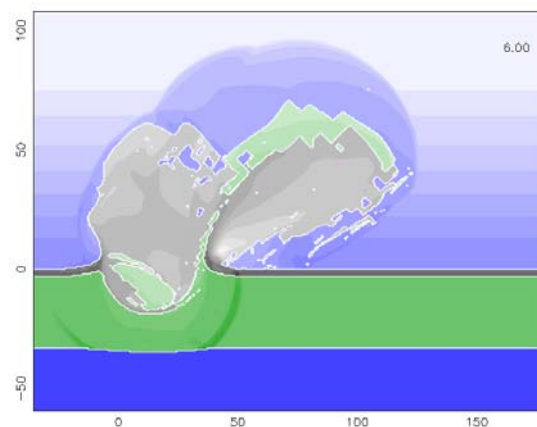


Fig 3. Six seconds after a 45-degree impact. Shock wave in the target reaches the mantle, shock wave in atmosphere is above 80 km. The vapor plume consists of vaporized-molten sediments (gray color) and projectile (green). Crystalline basement is not involved in the ejecta.

Acknowledgments. N. A. is supported by RFBR grant 01-05-64564-a, the Berlin group by DFG grants Sto 101/38-1 and Ke 732/8-2.

References. [1] Dressler et al. (2003) *EOS* 84, 125, 130. [2] Stöffler et al. (2003) LPS XXXIV, Abstract # 1553. [3] Tuchscherer et al. (2003) LPS XXXIV, Abstract # 1310. [4] Ivanov B. et al. 2003, this volume. [5] Hecht et al. (2003) LPS XXXIV, Abstract # 1583. [6] Shuvalov V. (1999) *Shock Waves* 9, 381-390. [7] Thompson S. L. and Lauson H.S. (1972) *SC-RR-61 0714*, 119 p. [8] Morgan J. et al (1997) *Nature*, 390, 472–476. [9] Pierazzo et al. (1997) *Icarus* 127, 498-523. [9] Tagle et al. (2003) LPS XXXIV, Abstract # 1811.

A NEW VIEW OF MARTIAN IMPACT CRATERS. N. G. Barlow, Dept. Physics and Astronomy, NAU Box 6010, Northern Arizona University, Flagstaff, AZ 86011-6010 USA Nadine.Barlow@nau.edu

Introduction: The Mars Global Surveyor and Mars Odyssey instruments have acquired a plethora of new information about martian impact craters. The combination of high resolution multispectral images, topography, mineralogy, and thermal inertia has expanded our understanding of the morphologic and morphometric variations associated with martian impact craters. The new data are allowing us to investigate the formation mechanisms of craters and their associated features in a level of detail previously unavailable.

Image Data: Viking Orbiter imagery covered the entire planet at resolutions between 40 and 100 m/pixel. While a few areas were imaged at higher resolutions, many other regions, particularly at higher latitudes, were imaged very poorly due to clouds. The Mars Orbiter Camera (MOC) system on Mars Global Surveyor (MGS) obtains resolutions of up to 2 m/pixel using the narrow angle (NA) camera. MOC allows very detailed analysis of features in selected regions of the planet. Mars Odyssey's (MO) Thermal Emission Imaging System (THEMIS) provides the intermediate resolutions necessary to provide the geologic context between the lower resolution Viking and the high resolution MOC data. The THEMIS visible (VIS) camera images have 18 m/pixel resolution. The THEMIS infrared (IR) camera has 100 m/pixel resolution but is providing new insights into crater properties such as rock distribution. In addition THEMIS IR imagery allows us to compare day-night images of the same areas and is less affected by the clouds often hampering views of the higher latitudes.

Topography: The Mars Orbiter Laser Altimeter (MOLA) instrument on MGS has provided the first detailed topographic data for the planet. MOLA has a vertical accuracy of 1 m over a surface spot size of 168 m (from the 400-km-elevation mapping orbit) [1]. As a result, MOLA has been able to provide highly accurate measurements of crater morphometric features such as crater depth, rim height, crater volume, ejecta thickness, and distal rampart height. Measurements have been made using center line profiles [2] and the gridded digital elevation maps [3]. These studies show that craters at high latitudes display statistically different morphometries than craters at near-equatorial latitudes [2]. In addition, distal ramparts seem to be ubiquitous for non-pedestal layered ejecta morphologies regardless of whether such a rampart is seen in image data [4].

Mineralogy and Thermal Inertia: Detailed mineralogic information for individual craters is not yet available from THEMIS, but regional mineralogy has been derived from the MGS Thermal Emission Spectrometer (TES), which has a spatial resolution of 3 km [5]. Additional mineralogic information is being provided by MO's Gamma Ray Spectrometer (GRS), but the 300-km-size footprint of these data prevent their use for anything but regional analyses. Thermal inertia (TI) has been determined using TES data [6], but additional insights are already being provided by THEMIS IR data, particularly the day-night image comparisons.

This Study: The *Catalog of Large Martian Impact Craters* was compiled in the 1980's from the Viking 1:2,000,000 photomosaic series. The *Catalog* contains information for 42,283 impact craters ≥ 5 -km-diameter distributed across the entire planet. Each entry contains information about the crater's location, size, terrain on which it is superposed, ejecta and interior morphologies (if applicable), preservation state, and angle of orientation if the crater is elliptical. We are currently revising the *Catalog* using the new insights gained from MGS and MO. In addition to updates to the existing *Catalog* entries, we are including the morphometric, mineralogic, and TI information provided by MOLA, TES, and THEMIS [7]. When completed, the revised *Catalog* will be accessible to the planetary community through the USGS GIS-based PIGWAD system (webgis.wr.usgs.gov) [8] and through the Planetary Data System.

The data are revealing important new insights into martian impact crater morphologies and morphometries. MOLA data are allowing us to confirm or deny the existence of previously reported basins on Mars [9] and to identify new, buried basins [10]. Clearer imagery of the polar regions, using THEMIS IR, is allowing us to verify and better classify previously mapped structures which were poorly imaged through clouds. The topographic data provided by MOLA are also being used to clearly define the extent of ejecta structures. The maximum extent of layered ejecta morphologies (called ejecta mobility ratio, or EM) is commonly believed to provide information about the viscosity of the ejecta debris cloud at the time of emplacement, which in turn provides information on the concentration of the fluidizing material [11, 12]. Our EM analysis confirms previous reports of a latitude dependence, with higher EM (more mobile ejecta) found at higher latitudes, but reveal differences

in EM values for different ejecta morphologies [13]. EM comparisons with crater preservation state suggest that there has been little temporal variation in the concentration of subsurface volatiles at the 100-meter to few-km depths excavated by these craters [14].

Three major types of layered ejecta morphologies have been identified on Mars: the single layer (SLE), double layer (DLE), and multiple layer (MLE) ejecta patterns [4]. We have used data in the revised *Catalog* to investigate regional variations in the distribution of these ejecta morphologies. We find that the DLE and MLE morphologies are concentrated in specific regions of the planet and that these locations correlate with many of the near-surface (<1-m depth) H₂O-rich regions reported by GRS [15] (Figure 1).

Two major theories exist for the formation of the layered ejecta morphologies surrounding fresh martian craters: vaporization of subsurface volatiles during impact [16] and interaction of the ejecta column with the thin martian atmosphere [17]. Modeling of the two processes has now advanced to a stage where slight differences in the expected crater morphology are now seen between the models [17, 18]. The detailed image and topographic data for martian impact craters allows us to now compare the fine detail observed in these craters with those features predicted by the two primary formation models. We are beginning such a study and will report on preliminary results at the meeting.

References: [1] Smith D. E. et al. (2001) *JGR*, 106, 23689-23722. [2] Garvin J. B. et al. (2000) *Icarus*, 144, 329-352. [3] Mouginis-Mark P. J. et al. (2003) *LPS XXXIV*, Abstract #1472. [4] Barlow N. G. et al. (2000) *JGR*, 105, 26733-26738. [5] Christensen P. R. et al. (2001) *JGR*, 106, 23823-23871. [6] Mellon M. T. et al. (2000) *Icarus*, 148, 437-455. [7] Barlow N. G. (2000) *LPS XXXI*, Abstract #1475. [8] Barlow N. G. et al. (2003) in *Advances in Planetary Mapping, ISPRS WG IV/9: Extraterrestrial Mapping Workshop*, Houston, TX. [9] Schultz P. H. et al. (1982) *JGR*, 87, 9803-9820. [10] Frey H. et al. (2002) *GRL*, 29, 10.1029/2001GL013832. [11] Mouginis-Mark P. J. (1979) *JGR*, 84, 8011-8022. [12] Costard F. M. (1989) *Earth Moon & Planets*, 45, 265-290. [13] Barlow N. G. and A. Pollak (2002) *LPS XXXIII*, Abstract #1322. [14] Barlow N. G. (2003) *LPS XXXIV*, Abstract #1122. [15] Barlow N. G. and C. B. Perez (2003) *JGR* in press. [16] Carr M. H. et al. (1977) *JGR*, 82, 4055-4065. [17] Barnouin-Jha O. S. and P. H. Schultz (1998) *JGR*, 103, 25739-25756. [18] Stewart S. T. et al. (2001) *LPS XXXII*, Abstract #2092.

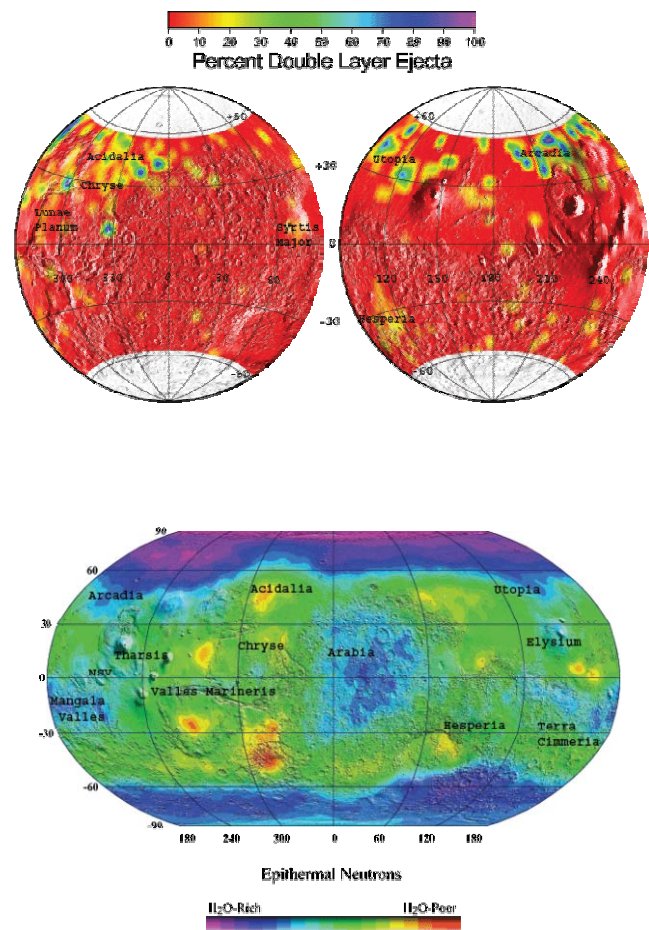


Figure 1: Comparison of the distribution of craters displaying the double layer ejecta (DLE) morphology (top) with the distribution of near-surface H₂O as determined by GRS (bottom). Highest concentrations of craters and H₂O are shown in greens, blues, and purples. The high latitude regions of Acidalia, Arcadia, and Utopia show the highest concentrations of DLE morphology craters. Arcadia and Utopia show high concentrations of H₂O in the GRS map. This suggests that although the craters excavate to greater depths than the depth penetrated by GRS, there may be communication of volatiles between these regions. Acidalia shows as an H₂O-poor region in this GRS map, but Acidalia was still covered by CO₂ ice at the time this map was produced. More recent results suggest that Acidalia is also rich in H₂O. (GRS map courtesy of W. Boynton and the GRS team.)

EFFECTS OF PRE-EXISTING TARGET STRUCTURE ON THE FORMATION OF LARGE CRATERS. *O.S. Barnouin-Jha*¹, *M.J. Cintala*², and *D.A. Crawford*³, ¹JHUAPL, Laurel, MD; ²NASA JSC, Houston, TX; ³Sandia National Labs., Albuquerque, NM.

Introduction – The shapes of large-scale craters and the mechanics responsible for melt generation are influenced by broad and small-scale structures present in a target prior to impact. For example, well-developed systems of fractures often create craters that appear square in outline [1], good examples being Meteor Crater, AZ [2] and the square craters of 433 Eros (Fig. 1).

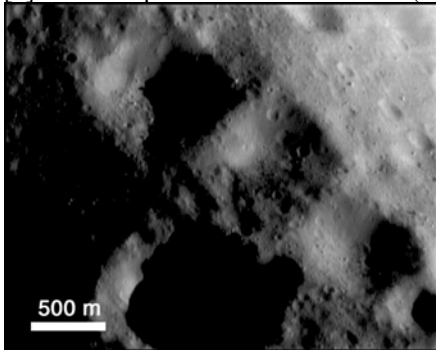


Figure 1. Square craters visible on the surface of 433 Eros formed between pre-existing tectonic ridges.

Pre-broken target material also affects melt generation. Kieffer [3] has shown how the shock wave generated in Coconino sandstone at Meteor crater created reverberations which, in combination with the natural target heterogeneity present, created peaks and troughs in pressure and compressed density as individual grains collided to produce a range of shock mineralogies and melts within neighboring samples.

In this study, we further explore how pre-existing target structure influences various aspects of the cratering process. We combine experimental and numerical techniques to explore the connection between the scales of the impact generated shock wave and the pre-existing target structure. We focus on the propagation of shock waves in coarse, granular media, emphasizing its consequences on excavation, crater growth, ejecta production, cratering efficiency, melt generation, and crater shape. As a baseline, we present a first series of results for idealized targets where the particles are all identical in size and possess the same shock impedance. We will also present a few results, whereby we increase the complexities of the target properties by varying the grain size, strength, impedance and frictional properties. In addition, we investigate the origin and implications of reverberations that are created by the presence of physical and chemical heterogeneity in a target.

Background: Hints as to how pre-existing target structures affect crater growth and ejecta excavation can be obtained from existing experimental data [4,5,6,7], numerical efforts [8] and observations [1,2]. Classic experiments [1] indicate that impacts into targets with pre-existing faults cause azimuthal variations in ejecta thickness and changes in the final crater appearance. More

recent experimental work [5,6,7] and numerical calculations [8] indicate that impacts into pre-fractured or granular targets, which resemble a rubble-pile asteroid, cause little additional fragmentation; instead, the ejected fragments simply gain more kinetic energy, especially near the impact point, and the shock wave decays more rapidly.

These various studies suggest that the size of particles comprising a target might somehow influence crater growth. A reasonable factor to consider is the thickness of the shock front w relative to the average dimension d of those grains.

In the following sections, we explicitly investigate how the shock-pulse thickness relative to target grain-size might influence shock-pulse decay, ejecta excavation and crater growth. First, we compare simple estimates of shock thickness with old [1] and new experimental results for crater growth and ejecta excavation. Second, we perform some idealized numerical calculations of identical projectiles impacting a variety of spherical targets.

It should be noted that that the presence of heterogeneity in the target will always affect the cratering process, regardless of scale. For example, a target composed of a mixture of two minerals will propagate a shock in a very different manner than a monomineralic target, with subsequent consequences on crater growth and ejecta excavation regardless of the shock's thickness. However, shock-thickness effects will be enhanced when their scales compare favorably with pre-existing target heterogeneities.

Estimating shock-wave thickness: In order to compare shock-wave thickness to changes in the cratering process, we need a measure of this wave thickness. Currently, direct measurements of the shock-pulse thickness are not possible during our experiments. However, numerical calculations show that a reasonable first order estimate of w is obtained from hydrodynamic impact theory [e.g. 9] by

$$w = \frac{2a}{U_p} (U_t - u_t)$$

where U_t and U_p are the speeds of the shock wave in the target and projectile respectively, u_t is the material velocity in the target after passage of the shock and a is the diameter of the projectile.

The thickness w can be changed in two ways. Changing the diameter a of the projectile is by far the easiest way: the greater the projectile diameter, the greater w becomes. Changing the projectile's impact velocity is the second way of achieving a change in pulse thickness. Usually, for a fixed projectile diameter, the shock pulse would be longer at lower impact velocities and shorter at higher ones.

Laboratory and Numerical investigations: We compare the just-derived wave thickness w to results obtained both in the laboratory and through numerical modeling to investigate the influence of pre-existing target structures on the cratering process. At the time of this abstract, we had undertaken two sets of impact experiments. In the first, we investigated the effects of changing impact velocity by launching a 4.8mm Al projectiles between 0.8 and 1.92km/s into a coarse 1-3mm sand target. In the second, we launch a 0.32mm projectile at 0.42 km/s into fine 0.25 mm sand. In both sets of experiments, we measure the velocity of individual grains using a laser-strobe technique. In the second experiment, we also measure crater growth times. From these measurements, we obtain the exponent e_x that defines the decay of velocities of ejecta from craters formed under gravity-dominant conditions according to the scaling protocol of [10]. A greater value of e_x implies more rapid decay; conversely, a lower value implies less rapid decay.

The numerical investigations were performed with the Eulerian shock code CTH [11] using the adaptive mesh refinement technique. We begin with several highly idealized impact calculations where the targets were strengthless quartz, with individual grains that flow rather than slip past each other. A 2-D axisymmetric geometry was used, where the coarse-grained targets are actually composed of one central sphere surrounded by many circular tori with equivalent diameter. In these calculations, we change the size of the projectile and monitor crater growth for given coarse-grained targets to obtain e_x .

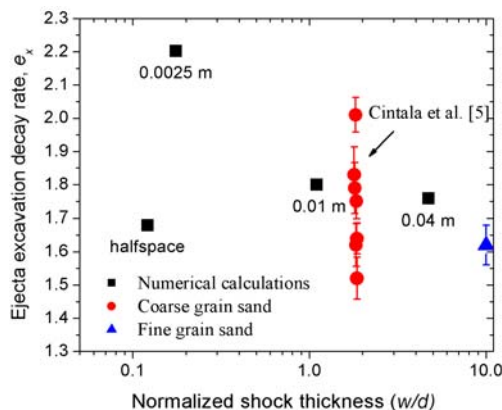


Figure 2. Ejecta excavation decay rate e_x as a function of normalized shock thickness w/d found from experiments and numerical investigation. The value of w/d used for the continuous halfspace target (labeled halfspace) was taken to be small since d is infinitely large relative to w .

Results: Figure 2 plots e_x against w/d obtained from laboratory experiments and numerical calculations. If the target grains exert no influence on the rate of shock wave attenuation and, hence, on cavity excavation, then e_x should be independent of impact velocity. However, if these grains do influence shock attenuation, when w

approaches d (i.e., $w/d \sim 1$) crater growth should be significantly influenced by the grains, yielding rapid decays in the velocities of ejecta; conversely, waves that are far larger ($w/d \gg 1$) or smaller ($w/d \ll 1$) than the grains should decay more slowly. In these latter two cases, the value of e_x should begin to approach the value expected for halfspace targets. Figure 2 clearly shows not only that grain size influences the decay of ejecta excavation velocity, but that, as the shock grows in size, e_x approaches values measured in the laboratory for impacts into fine 0.25-mm sand, and computed numerically for impacts into a continuous strengthless halfspace target. The experimental results for the coarse-grained target show a very impressive decrease in the values of e_x for a small change in w/d around 1. These data also indicate some variability in the values of e_x for w/d that are very nearly equal. This variability could indicate differences in early time interactions between the projectile and the coarse target grains.

We will report additional results obtained from impact experiments and numerical studies we are currently conducting. In these, we continue to alter target grain size, projectile size and velocity. We will also investigate how impact geometry (changes in the location where the projectile first strikes the grains in coarse-grained target), particle friction, and particle strength may play a role in shock propagation and subsequent crater-formation processes. These studies will provide further insight into the relationships between shock-pulse thickness, the target's grain size, and its strength on decay of the shock pulse, ejecta excavation, and crater growth.

References:

- [1] Fulmer, C.V. and W. A. Roberts, *Icarus* 2, 452-465, 1963.
- [2] Shoemaker, E.M., In *The Moon, Meteorites and Comets*, Univ. of Chicago Press, Chicago, 1963.
- [3] Kieffer, S.W., *Jour. of Geophys. Res.*, 76, 5449-5473, 1971.
- [4] Gault, D.E., Quaide, W.L., and V. R. Oberbeck, In *Shock Metamorphism of Natural Materials*, Mono, Baltimore, MD, 87-100, 1968.
- [5] Cintala M.C., L. Berthoud and F. Hörz, *Meteorit. Planet. Sci.*, 605-625, 1999.
- [6] Ryan, E.V., W.K. Hartmann and D.R. Davis 1991, *Icarus* 94, 298-298.
- [7] Martelli, G., E.V. Ryan, A.M. Nakamura and I. Giblin, *Planet Space Sci.* 42, 1013-1026.
- [8] Asphaug, E., S.J. Ostro, R.S. Hudson, D.J. Scheeres and W. Benz, *Nature* 393, 437-440, 1998.
- [9] Gault, D.E. and Heitowit, E.D. *Proceedings, Sixth Hypervelocity Impact Symposium* 2, 419-456
- [10] Housen, K.R., R.M. Schmidt and K.A. Holsapple, *J. Geophys. Res.* 88 (B3), 2485-2499, 1983
- [11] McGlaun, J.M., S.L., *Int. J. Impact Eng.*, 10, 351-360, 1990.

THE IMPACT RATE OF SMALL ASTEROIDS AT THE EARTH'S SURFACE. P. A. Bland¹ and N. A. Artemieva², ¹Department of Earth Science and Engineering, Exhibition Road, Imperial College London, South Kensington Campus, London SW7 2AZ, UK, p.a.bland@imperial.ac.uk; ²Institute for Dynamics of Geospheres, Russian Acad. Sci., Leninsky Prospect 38/6, Moscow, Russia 117939, nata_art@mtu-net.ru.

Introduction: The craters preserved on the lunar mare provide a record of the rate of impacts and the impactor size distribution, over a mass range of $\sim 10\text{--}10^{16}$ kg, for the 3.2-3.5Ga since the mare basalts were emplaced [1]. Constructing a similar curve for number of impacts over a given mass at the Earth's surface is complicated: the atmosphere disrupts meteoroids [2], and craters are removed by erosion and tectonism, infilled, or simply go unrecognised. A combination of these factors has given rise to the long-recognised departure from a simple power-law size distribution for terrestrial craters <20km in diameter [3]. Since the terrestrial small crater record is incomplete, and inadequate for constraining the flux at the surface, we have chosen to scale the known impact rate at the upper atmosphere to a flux at the surface by modelling how a given bolide behaves in the atmosphere.

Understanding the atmosphere-bolide interaction is crucial to determining a flux at the surface, but accurately modelling the fragmentation and ablation behaviour of bodies with different strength, composition, and mass, is a non-trivial task. Although there were early attempts to model separated impactor fragments [4,5], most subsequent semianalytical approaches have simplified the problem by considering the impactor as a strengthless liquid-like object: so-called 'pancake' models, in which clouds of fragments are modelled as a continuous, lower-density, deformed impactor [2,6-8]. Unfortunately, although 'pancake' models are of value in delineating, for example, the height at which bolides disrupt (e.g. [6]), they are not capable of reproducing the cratering behaviour of fragmented asteroids at the Earth's surface. In contrast, Artemieva and co-workers [9-11] have developed a model that calculates motion, aerodynamic loading, and ablation, for each individual particle or fragment. We have used the separated fragments (SF) model to understand fragmentation and ablation in the Earth's atmosphere for a range of impactor types and masses, in addition to a 'pancake' model [6], and a simple ablation model. The benefit of the SF approximation is that it allows us to define a mass-velocity distribution at the surface for solid fragments which either create craters (in the case of high final velocity) or which may be found as meteorites (fragments with low final velocity) ie. for a given impactor at the top of the atmosphere, it allows us to predict the mass-velocity-distribution for that impactor at the Earth's surface. The flux at the upper atmosphere has recently been well constrained over a

large portion of the mass range [12-19]. In addition, asteroid spectroscopy [20-23] and impactor composition in large terrestrial craters [24] place constraints on the composition of the flux at the top of the atmosphere. A knowledge of the fragmentation and ablation behaviour for a given initial mass and impactor type allows us to estimate the energy and mass delivered to the surface, so that the flux curve for the upper atmosphere can be scaled to an impact rate at the Earth's surface.

Methodology: The SF model used here has been developed over several years, and is based on 3D hydrocode modelling [9,10]. It is described in detail elsewhere [10,11]. The model takes into account successive fragmentation and ablation of individual fragments. The meteoroid is subjected to disruption if dynamic loading exceeds tensile strength, which depends on the projectile type and size. The model simulates the evolution of a meteoroid consisting of a variable number of solid fragments. The number of fragments changes in the process of the calculation from 1 to an arbitrary value, depending on the properties of individual fragments. Fragments have higher strength than the initial body, but may be disrupted again later into a new pair, etc. The equation of motion [4] is solved for each individual fragment, with an additional equation describing repulsion. The cross-range spread is produced by the interaction of bow shocks after breakup, spreading velocity U (two identical fragments with density ρ_b , trajectory velocity V disrupted at the altitude with atmospheric density ρ_a) is defined as $U = CV(\rho_a/\rho_b)^{0.5}$ with $C=0.01\text{--}1$ from the analysis of the Earth's strewn fields. The idea is confirmed in 3D modelling of disrupted meteoroid motion [9,10]. The coefficient of repulsion C is defined as 0.45.

Two types of projectile are principally considered: irons with density of 7800kg/m^3 , ablation coefficient of $0.07\text{ s}^2/\text{km}^2$ and strength of $4.4 \times 10^8\text{ dyn/cm}^2$ (for 1kg sample) [10], and stones with density of 3400kg/m^3 , ablation coefficient of $0.014\text{ s}^2/\text{km}^2$ and 10x lower strength. The parameters for stones were chosen to define approximate upper limits on strength and density: larger stony bodies in the atmosphere, and carbonaceous bolides, may well have significantly lower strength and density. We performed 16 simulations for stony impactors using the SF model, and 16 for irons, for bodies from 1 to 10^8kg , repeating each simulation for a given mass >20 times to derive aver-

age impact conditions (in total >1000 SF model simulations were performed). ‘Pancake’ model simulations were performed over the range 1-10¹²kg. All simulations were at average asteroidal impact velocities and entry angles: 18 km/s and 45° respectively.

Results and discussion: When the model outputs are compared we find that ‘pancake’ and SF model estimates of total surviving material at the surface coincide tolerably well for irons, but the same is not true for stones. A ‘pancake’ model with spreading to x2 initial radius is typically chosen, which significantly overestimates impactor survivability for stones over the whole mass range. SF and ‘pancake’ results only converge when we consider spreading to x4 initial radius (much larger than typically used) and only for initial masses >10⁷kg (possibly as larger stones behave as a liquid-like ‘swarm’ of fragments).

SF modelling also quantifies the dramatically different survivability of iron and stony impactors. Over the mass range 10³-10⁷kg iron impactors transfer to the surface ~3 orders-of-magnitude more energy/unit area than stones: a fragmented iron impactor of 10⁵kg produces a similar crater-field to a fragmented 10⁸kg stone (Figure 1). Even larger stony bodies of ~10⁸-10¹⁰kg are much less efficient at transferring energy to the surface

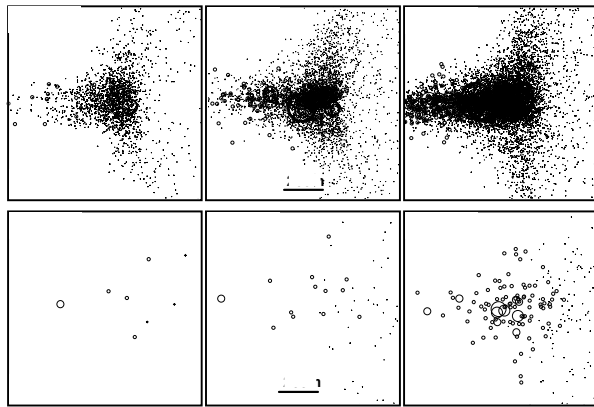


Figure 1. Crater fields for iron (top row) and stony (bottom row) bodies for a range of pre-entry masses. Sizes of circles approximately equal the size of impact craters - dots are for <10m pits. For stones, although a small percentage of the impactor reaches the surface, even a 10⁸kg mass does not lead to impact crater formation.

than the equivalent iron impactor. SF model simulations constrain the mass-velocity-distribution of these fragments, allowing us to derive morphologies of simulated crater fields. The SF results are in good agreement with terrestrial crater records, and also with available meteorite data.

A compilation of flux data for the top of the

Earth’s atmosphere [12-19] is found to match the size-frequency distribution of impactors derived from the lunar mare crater record [25,26] (after crater data is scaled to projectile diameter [27,28]) to within a factor of 3 over 16 orders of magnitude. We therefore take this curve for our flux at the upper atmosphere, and scale it to a flux at the surface based on our database of impact simulations and an estimate of impactor composition at the upper atmosphere [20-24].

Conclusion: This analysis constrains the impactor flux at the Earth’s surface over the mass range 10²-10¹²kg. Our data indicate a significantly lower surface flux than some previous studies have suggested [29].

References: [1] Hartmann W.K. *et al.* (1981) in *Basaltic Volcanism on the Terrestrial Planets* (Pergamon Press, New York), 1050. [2] Melosh H.J. (1981) in *Multi-Ring Basins* (Pergamon Press, New York), 29. [3] Grieve, R.A.F. Shoemaker E.M. (1994) in *Hazards due to Comets and Asteroids*, Gehrels T., Ed. (Univ. Arizona Press, Tucson), 417. [4] Passey Q.R., Melosh H.J. (1980) *Icarus* 42, 211. [5] Melosh H.J. (1989) *Impact Cratering: A Geological Process* (Oxford University Press, Oxford). [6] Chyba C.F., Thomas P.J., Zahnle K.J. (1993) *Nature* 361, 40. [7] Hills J.G., Goda M.P. (1993) *Astron. J.* 105, 1114. [8] Hills J.G., Goda M.P. (1998) *Planet. Space Sci.* 46, 219. [9] Artemieva N.A., Shuvalov V.V., *Shock Waves* 5, 359 (1996). [10] Artemieva N.A., Shuvalov V.V. (2001) *J. Geophys. Res.* 106, 3297. [11] Shuvalov V.V., Artemieva N.A., Trubetskaya I.A. (2000) *Solar System Research* 34, 49. [12] Halliday I., Griffin A.A., Blackwell A.T. (1996) *MAPS* 31, 185. [13] Nemtchinov I.V. *et al.* (1997) *Icarus* 130, 259. [14] Brown P. *et al.* (2002) *Nature* 420, 294. [15] ReVelle D.O. (1997) *Ann. NY Acad. Sci.* 822, 284. [16] Morbidelli A. *et al.* (2002) *Icarus* 158, 329. [17] Rabinowitz D. *et al.* (2000) *Nature* 403, 165. [18] Stuart J.S. (2001) *Science* 294, 1691. [19] Harris A.W. (2003) in *Proc. Asteroids, Comets, Meteors 2002* (Berlin, in press). [20] Burbine T.H. (2002) *Bull. Czech Geol. Surv.* 77. [21] Bus S.J., Binzel R.P. (2002) *Icarus* 158, 146. [22] Binzel R.P. *et al.* (2003) in *Asteroids III*, Bottke W.F. *et al.*, Eds. (Univ. Arizona Press, Tucson), 255. [23] Tholen D. J. (1989) in *Asteroids II*, Binzel R.P., Gehrels T., Matthews M.S., Eds. (Univ. Arizona Press, Tucson) 1139. [24] Earth Impact Database <http://www.unb.ca/passc/ImpactDatabase/> (Accessed November 20th 2002). [25] Ivanov B.A. *et al.* (2003) in *Asteroids III* Bottke W.F. *et al.*, Eds. (Univ. Arizona Press, Tucson), 89. [26] Hartmann W.K. (1999) *MAPS* 34, 167. [27] Schmidt R.M., Housen K.R. (1987) *Int. J. Impact Engng.* 5, 543. [28] Ivanov B.A. (2001) in *Chronology and Evolution of Mars*, Kallenbach R. *et al.*, Eds. (Kluwer, Dordrecht) 87. [29] Ward S.N., Asphaug E. (2000) *Icarus* 145, 64.

THE EASTERN HUDSON BAY ARC, CANADA: PART OF A MULTI-RINGED IMPACT BASIN.

Michael E. Brookfield, Land Resource Science, Guelph University, Ontario N1G 2W1, Canada.
mbrookfi@lrs.uoguelph.ca

Almost 35 years ago, Beals [1] proposed an impact origin for the great eastern arc of Hudson Bay, which extends for almost 650 kilometres through an angle of 155 degrees and has a coherent circular raised rim on its landward side. A rift extends at right angles outwards on the southeastern side and within the arc, the basin is filled with Proterozoic sediments. The best fit circle has a radius of 230 kilometres and the arc deviates from this circle by less than 10 km along its entire length. More recently, Goodings and Brookfield [2] noted that closing the James Bay rift aligns the Sutton ridge to form an arc of 240 degrees, or two-thirds of a circle (fig. 1). The remainder is cut by the younger circular northern James Bay cratonic basin.

Apart from impact, no other plausible explanation has been proposed for this great ring fracture (and another ring fracture may exist outside this one). But, because no definitive evidence of impact was found, little has been published on the Hudson Bay arc since 1968. Recent studies of multi-ringed basins on other planets, and of other large, old, multi-ringed basin, such as Vredefort, on Earth, provide criteria for re-investigation and re-interpretation of published reports. Along the Hudson Bay arc, bodies of pseudotachylite, monomict and exotic breccias are associated with faults, and overlying sediments may show evidence of re-worked impact melts.

If ongoing investigations are positive, Hudson Bay arc would form part of the largest identified multi-ringed impact on Earth, with a minimum diameter of 450 kilometres.

[1] Beals, C. S. (1968.) In: Beals, C.S. (editor), Science, History and Hudson Bay, volume 2. Department of Energy Mines and Resources, Ottawa., 985-999.

[2] Goodings, C.R. and Brookfield, M.E. (1992) *Earth-Science Reviews*, 32, 147-185.

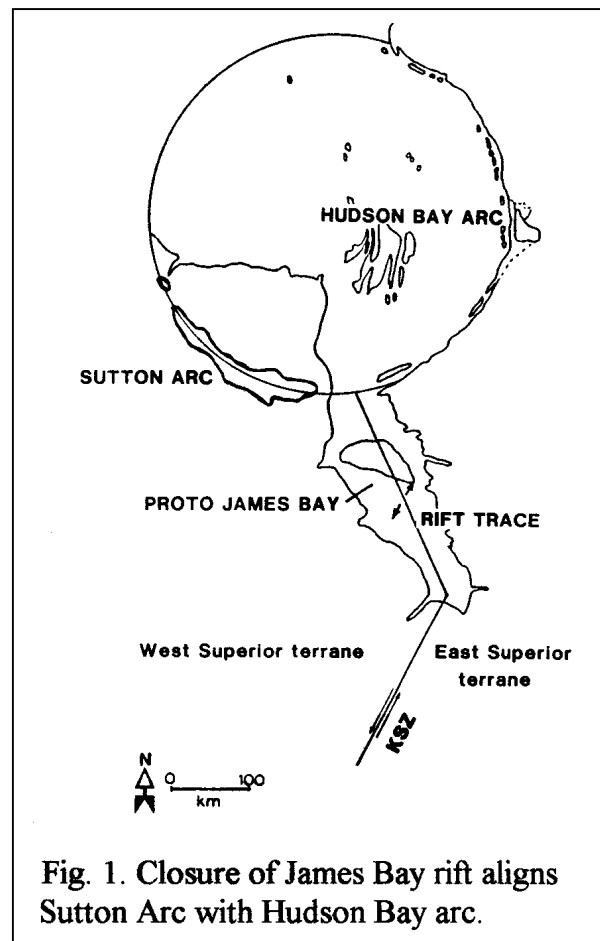


Fig. 1. Closure of James Bay rift aligns Sutton Arc with Hudson Bay arc.

EFFECT OF THE SUPPOSED GIANT IMPACT CRATER ON THE GEOLOGIC EVOLUTION OF THE URAL MOUNTAIN RANGE. G. A. Burba, Laboratory of Comparative Planetology, Vernadsky Institute of Geochemistry and Analytical Chemistry, 19 Kosygin St., Moscow 119991, Russia e-mail: burba@online.ru

Introduction: At the eastern outskirts of the European part of Russia there are the Ural Mountains, which marks the border between Europe and Asia. This mountain range have in general the straight linear position N to S along 60° E meridian. Such position changes abruptly within the middle segment of the range, between 54 and 59° N, where the mountain chains curves eastward along the semicircular outline. Such change looks to be caused by some obstacle, the lithospheric heterogeneity.

This eastward-looking arc of the Middle Ural Mountains is considered here as an eastern segment of a large ring structure, which is referred hereafter as Middle-Ural Ring Structure (MURS). The structure is located between 54 and 59°, 52 and 62° E. The minimal diameter of its rim is 400 km.

Surface topography: The eastern half of the MURS rim is a part of the Ural Range from Yamantau Mountain in the south to the area of Kachkanar Mountain in the North. NW part of the rim is Okhanskaya Vozvyshennost (Highland) to the North of Kama river. Western part is Sarapulskaya Vozvyshennost. SW part is Bugulminsko-Belebeyevskaya Vozvyshennost (to the South of Belaya river). There are two uplands in the central part of the MURS, both are N to S elongated: Tulvinskaya Vozvyshennost and Sylvinskiy Kryazh (Range). The SE part of the MURS bottom is occupied with Ufimskoye Plateau.

The topographic level of the eastern segment of MURS rim is up to 1000-1500 m above sea level, NW segment – up to 300 m, W segment – up to 200-250 m, SW – up to 300-350 m. The uplands in the central part of MURS are up to 400-450 m. Minimal altitude within the MURS is 58 m (in Kama river valley, near Belaya river mouth), and maximal is 1640 m (Yamantau Mountain on the south rim of MURS).

River net patterning: The ring of MURS is outlined inside with a general pattern of the large river valleys of Chusovaya, Belaya, and Kama river (the segment between the mouths of Chusivaya and Belaya, the left tributaries of Kama). Valleys of a smaller (intermediate-sized) river valleys also outline a MURS concentric patterning. The directions of small-sized rivers (being generalized to rectilinear positions) are mainly radial to MURS. So, the concentric-radial (so named ‘broken plate’) structure take place within the MURS.

Basement topography: There is an isometric depression in the basement under the MURS. Its depth is down to –8 km. There are two uprisings of the basement with summits located at –3 km depth. These uprisings are located just under the two uprisings in the surface topography within the central area of the MURS. The depth to diameter ratio for the depression of the basement is 1/50.

Paleoenvironment: Paleogeographical maps show the depression of the surface within the outlines of the MURS beginning from Precambrian time.

Mineral resources: The overwhelming majority of the mineral fields of the Ural Mountains are concentrated within the MURS, to put it more precisely, within the eastern half of its rim. There are ore fields of iron, copper, chromite, nickel, tungsten, gold, and some other metallic mineral resources here, as well as of the well-known Ural gems. One could say, that the mining industry of the Ural is in intimately connection with MURS. So, MURS makes the industrial power of the Ural.

Interpretation: The whole set of the data provides a possibility to conclude that the MURS have a structure, which looks like a giant impact crater, similar to the craters on the other planets. This crater have a sharp expression in the basement topography, and not so sharp expression in the surface topography. Such smoothing view of the surface topography could be connected with a thick layer of sediments, which have filled the crater. Uprisings in the central part of the MURS could be considered as places of the crater’s central mountains, as they are located over the basement uprisings. The mineral fields looks to be in connection with the activity within the presumable ring faults of the structure’s rim.

Conclusion: It could be suggested that the geologic evolution of the Middle Ural area took place within the net of faults, which have been originated during the impact event in Precambrian time and stay active during the further periods of geologic history. It looks like that MURS have been a stable obstacle during the formation of the Ural Mountains, so the ranges could not overpass through the MURS and changed their rectilinear propagation to circle the MURS from the east. MURS could be an ancient giant impact crater, which affected the geologic development of the Ural Mountains linear range.

GEOCHEMISTRY OF ACCRETIONARY LAPILLI FROM A CRETACEOUS-TERTIARY IMPACT BRECCIA, GUAYAL, MEXICO. E. Burns¹, H. Sigurdsson¹, S. Carey¹, S. D'Hondt¹¹Graduate School of Oceanography, University of Rhode Island

Introduction: Accretionary lapilli are found in a 50-cm-thick grit unit that is 2.5 m below the top of a fining-upward, 35-m-thick impact breccia near Guayal, southeastern Mexico. They were first described in 2000 by Salge et al. [1]. The breccia is thought to be associated with the Cretaceous-Tertiary Chicxulub impact on Yucatán. It is about 600 km from the crater center and consists of carbonate clasts in a carbonate-smectite matrix. The smectite is the alteration product of impact glass. The accretionary lapilli are rounded and flattened, with the long axis lying parallel to bedding (Fig. 1). Average dimensions of a set of 24 lapilli, measured with calipers, are 1.3 x 1.1 x 0.8 cm (s.d. = 0.19, 0.14, and 0.16), with an average aspect ratio of 0.59 (s.d. = 0.13). They are the largest objects in the grit unit, which has carbonate clasts of <0.5 cm. The lapilli are about 90% silica and are medium grey in color, with a waxy luster on freshly broken or sawed surfaces. They appear to have been largely replaced by diagenetic chert, but retain the layered internal structure that is typical of accretionary lapilli (Fig. 2). The centers are amorphous. Outer layers contain angular mineral grains aligned tangentially to the curvature of the layers [1]. Quartz and pyroxene grains have been identified in thin section. The matrix is cryptocrystalline to amorphous, but layers tend to alternate between slightly coarser and finer textures.

Chemistry: Two lapilli were sawed in half, polished, and analyzed for major-element oxides by electron microprobe and for trace elements by laser-ablation ICP-MS. The electron microprobe lines followed the laser-ablation lines. Their REE patterns are very similar to those of whole-rock samples of the surrounding carbonate-smectite grit, but with more pronounced positive Ce and negative Eu anomalies and a slightly steeper slope from LREE to HREE (Fig. 3). The shape of the patterns does not vary between layers within the lapilli or between the two lapilli analyzed, but the cores are slightly more concentrated in REE than the outer layers, and the average REE concentrations in one of the lapilli were greater than in the other. To minimize the effects of silica dilution on more mobile elements, elemental ratios were used to compare the lapilli to impact glass and alteration smectite from Beloc, Haiti [2] and continental crust [3]. These ratios may be the result of diagenetic processes rather than impact processes. The lapilli do not consistently resemble continental crust, impact glass, or smectite in their elemental ratios or overall composition. CaO and MgO are enriched relative to other major oxides, particularly FeO. MgO/FeO values in the lapilli are 3.7 and 4.0, while MgO/FeO in continental crust, glass, and smectite ranges from 0.5-0.9. Heavy metal con-

centrations tend to be lower than those in continental crust, especially Cr, which is 0.01-0.02 ppm compared to 185 ppm in continental crust and around 20-30 for the impact materials. The lapilli are low in Nb, Ta, Rb, and Ba, although Nb/Ta, Rb/Sr, and Rb/Ba ratios are comparable to continental crustal values. The lapilli resemble the yellow impact glass in Zr/Ta and Hf/Ta. Their U/Th is very high, averaging 13 compared to 0.26 for continental crust, and they contain more than 20 ppm U. The black and yellow impact glasses contain an average of 1.24 and 1.10 ppm U respectively, and alteration smectite has 0.36 ppm [2].

Discussion: The accretionary lapilli were most likely formed in the part of the impact vapor cloud where water vapor condenses, i.e. at or below 100° C. Thus their isotherm may have been close to Guayal, 600 km from the crater center. The accretionary lapilli appear to have been extensively replaced by chert. REE are thought to be less mobile during chert replacement than most other elements [4], so the REE patterns may be the best available indicator of the composition of the debris/vapor cloud in which the lapilli formed. The patterns resemble bulk continental crust and probably reflect the composition of the crystalline crust under the impact site, which would contribute more REE overall than would carbonates. It is not known if the Ce and Eu anomalies are the result of conditions in the vapor cloud or of some diagenetic process. SEM analyses by Salge et al. [1] show an average composition of 64% quartz, 19% clay minerals, 9% calcite, and 8% dolomite. The analyses done for this study gave considerably higher silica percentages and Ca and Mg percentages of ~3% or less of each. This could be because of differences among the lapilli or partly because of differences in analytical techniques, since this study did not include analysis of individual minerals or of carbonate. The U enrichment may be the result of U transport by diagenetic fluids from the surrounding carbonate rock into the lapilli during chert replacement.



Figure 1. Lapilli *in situ*, Guayal, Mexico. Divisions on measuring stick are 10 cm. Photo by H. Sigurdsson.

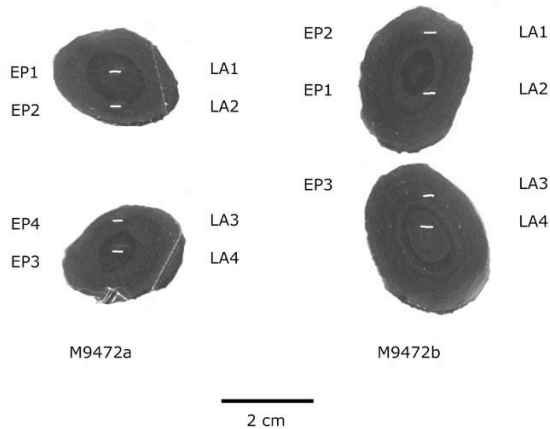


Figure 2. Lapilli in cross-section. Both sawed halves of each lapillus are shown. White lines indicate laser-ablation (LA)/ electron microprobe (EP) lines.

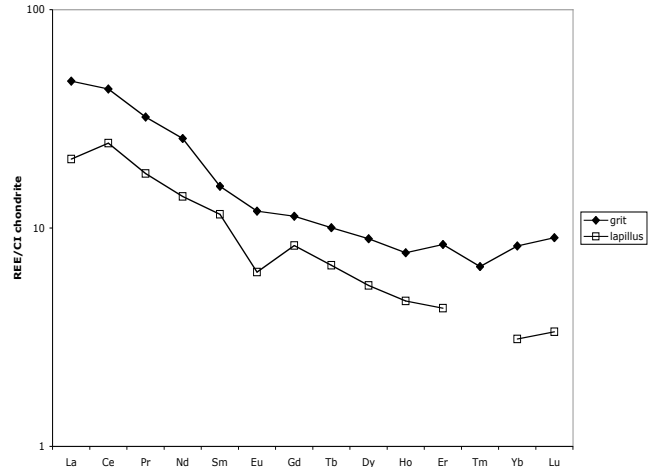


Figure 3. REE pattern of lapillus M9472a from the Guayal deposit compared to the surrounding grit. The lapillus pattern is the average of two laser-ablation lines in the center and two from outer layers. REE in the grit have been calculated on a carbonate-free basis to remove carbonate dilution effects. Samples are normalized to chondrite values from Anders and Grevesse [5].

References: [1] Salge, T. et al. (2000) *63rd Ann. Meteoritical Soc. Mtg.*, abs. 5124. [2] Koeberl, C., and Sigurdsson, H. (1992) *Geochim. Cosmochim. Acta*, 56, 2113-2129. [3] Taylor, S.R., and McLennan, S.M. (1985) *The Continental Crust: its Composition and Evolution*, Blackwell [4] Murray, R.W. (1994) *Sed. Geol.*, 90, 213-232. [5] Anders, E., and Grevesse, N. (1989) *Geochim. Cosmochim. Acta*, 53, 197-214.

NUMERICAL SIMULATIONS OF SILVERPIT CRATER COLLAPSE. G. S. Collins, B. A. Ivanov, E. P. Turtle and H. J. Melosh, Lunar and Planetary Laboratory, University of Arizona, Tucson, AZ 85721 (Email: gareth@lpl.arizona.edu).

Introduction: The Silverpit crater is a recently discovered, 60-65 Myr old complex crater, which lies buried beneath the North Sea, about 150 km east of Britain [1]. High-resolution images of Silverpit's subsurface structure, provided by three-dimensional seismic reflection data, reveal an inner-crater morphology similar to that expected for a 5-8 km diameter terrestrial crater. The crater walls show evidence of terrace-style slumping and there is a distinct central uplift, which may have produced a central peak in the pristine crater morphology. However, Silverpit is not a typical 5-km diameter terrestrial crater, because it exhibits multiple, concentric rings outside the main cavity.

External concentric rings are normally associated with much larger impact structures, for example Chicxulub on Earth, or Orientale on the Moon. Furthermore, external rings associated with large impacts on the terrestrial planets and moons are widely-spaced, predominantly inwardly-facing, asymmetric scarps. However, the seismic data show that the external rings at Silverpit represent closely-spaced, concentric fault-bound graben, with both inwardly and outwardly facing fault-scarps [1]. This type of multi-ring structure is directly analogous to the Valhalla-type multi-ring basins found on the icy satellites. Thus, the presence and style of the multiple rings at Silverpit is surprising given both the size of the crater and its planetary setting.

A further curiosity of the Silverpit structure is that the external concentric rings appear to be extensional features on the West side of the crater and compressional features on the East side [2]. The crater also lies in a local depression, thought to be created by post-impact movement of a salt layer buried beneath the crater [2].

The mechanics of Valhalla-type multi-ring basin formation: Theoretical and numerical modeling of multi-ring craters [3,4] suggests that external ring formation is a consequence of the basal drag exerted on a brittle, elastic surface layer by a more mobile substrate as it flows inwards to compensate for the absence of mass in the excavated crater. This model has been further constrained for Valhalla-type multi-ring basins. The formation of closely-spaced, concentric fault-bound graben, appears to require that the elastic upper layer be thin and that the mobile substrate be confined to a relatively thin layer [5,6,7]. This rheologic situation is easily explained in the context of the icy satellites; however, the presence of a thin highly mobile layer just below the surface is not a common occur-

rence on rocky bodies in the Solar System. In the case of the apparently unique Silverpit structure, it has been suggested that the mobile subsurface layer was caused by the presence of overpressured chalk layers at depth that acted as detachments and expedited inward flow of a thin subsurface layer [1].

Numerical Simulations: We have begun to test the proposed model for the formation of the Silverpit crater using three contrasting yet complementary numerical tools: SALES 2, SALEB and Tekton. SALES 2 is a Lagrangian hydrocode capable of modeling the dynamic collapse of large impact craters. It has been successfully applied to the problem of central peak and peak-ring formation [8]. SALEB is a multi-material Eulerian hydrocode, which has been used extensively for simulations of impact crater formation [9,10]. Both SALES2 and SALEB are direct descendents from the SALE hydrocode [11]. Tekton is a finite-element code designed to be applied to a wide range of tectonic problems, where displacements are relatively small and the dynamics are less important. It has been used extensively to simulate the relaxation of large craters and the formation of exterior rings in multi-ring basins [3].

Using SALEB, we investigate the formation of the Silverpit crater assuming an impact energy appropriate for forming a transient crater 3-km in diameter. Using SALES-2 and Tekton, we simulate the gravity-driven collapse of a bowl-shaped transient crater, 1-km deep and ~3-km in diameter. We model the target to a radial distance of >10 km and a vertical depth of 10 km to avoid boundary effects. All three of our models consist of three, originally-horizontal layers. For the SALES-2 and Tekton simulations these layers are deformed using the Z-model approximation of the excavation flow. The top two layers are assigned appropriate rheologic parameters to represent the brittle upper layer and the lower mobile layer at Silverpit. The bottom layer occupies the remainder of the mesh.

For simplicity in our early calculations, we assume that the target is compositionally homogeneous; we use the ANEOS equation of state for calcite in the SALEB calculations and the Tillotson equation of state for limestone in SALES-2. The important differences between the brittle upper layer and the mobile layer are rheologic. The mobile layer may be represented by an inviscid, or Newtonian fluid, or a fluid with a constant yield strength (Bingham fluid). The upper layer is modeled as an elastic-plastic solid with a pressure-dependent shear strength and a constant tensile strength, which are both degraded by damage. Damage

accumulation in shear is determined using a Johnson and Holmquist-type algorithm [12], where damage increases linearly with plastic strain up until the plastic strain at failure. At this point and beyond, damage is complete and the material is modeled as a cohesionless Coulomb material. Tensile damage is accumulated either using the Grady-Kipp model, for calculations in SALES-2 [13], or using a simple, single-flaw growth model in SALEB.

Results: Figure 1 shows the effect of the mobile middle layer on final crater structure and extent of the damaged region. In the simulation illustrated in the lower panel, the mobile layer was treated as a Bingham fluid with a small (5 bar) yield strength and a viscosity of 10^7 Pa s. The upper layer was modeled with an undamaged tensile strength of 10 MPa, a cohesion of 100 MPa and a coefficient of friction of 1.0 for undamaged material and 0.5 for completely damaged material. The plastic strain at failure was defined to be 1% at low confining pressures increasing to 10% at 100 MPa. The final crater has a diameter of 5-6 km with a well pronounced central uplift. The damaged region of the crater extends well away from the crater rim but is confined to the upper half of the brittle layer.

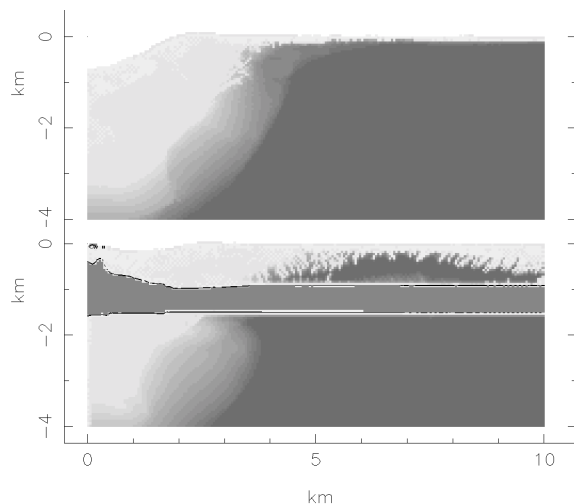


Figure 1: Comparison of the final crater structure and extent of damage (shading) for two axisymmetric SALEB simulations. The upper panel shows the result of an impact into a uniform target, the lower panel illustrates the effect of the weak mobile layer. In the lower panel the damaged region (shaded lighter) is much more extensive. The “crater rim” is at around 2.5-3 km radius in both cases, but in the lower panel the central region is slightly elevated.

To investigate the formation of the exterior rings at Silverpit we have also performed numerous crater collapse simulations. Figure 2 shows the results of one such model. In this case, the initial crater is a cylindrical hole with a radius of 3 km. During the simulation,

the mobile lower layer flows inward causing the elasto-plastic layer above to sag downward. The flexure in the brittle layer causes extensional faulting in the top half of the upper layer.

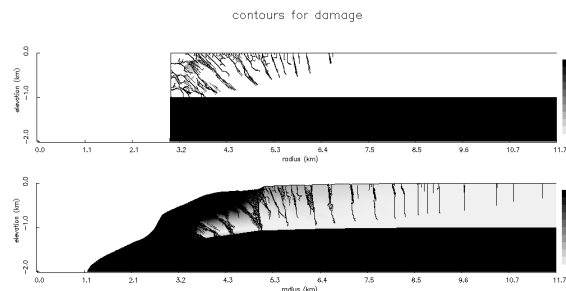


Figure 2: Close-up of a simple, axisymmetric two-layer collapse simulation performed using SALES-2. The shading denotes the amount of damage (black = completely damaged, white = undamaged).

Conclusions: Silverpit is a fascinating and unique terrestrial impact structure. The proposed model for the formation of the external rings at Silverpit is supported by our modeling results. Inward flow of the mobile middle layer causes flexure of the upper layer and produces extensional faulting in the top half of the upper layer. Results from our preliminary simulations suggest that the brittle upper layer must be ~1-km thick in order to reproduce observed fault patterns and the central uplift. The asymmetry in the nature of the external rings at Silverpit may be due to thickness variations in the mobile layer, or post-impact subsidence related to the salt movement. Further work is required to investigate this thoroughly.

References: [1] Stewart, S. A. and Allen, P. J. (2002) *Nature* 418, 520-523. [2] Allen, P. J. and Stewart, S. A. (2003) *LPSC XXXIV*. [3] Turtle, E.P., (1998) *Ph.D. Thesis, University of Arizona*. [4] Melosh, H. J. and McKinnon, W. B. (1978) *Geophys. Res. Lett.* 5, 985-988. [5] McKinnon, W. B. and Melosh, H. J. (1980) *Icarus* 44, 454-471. [6] Melosh, H. J. (1982) *JGR* 87, 1880-1890. [7] Allemand, P and Thomas, P. (1999) *JGR E* 104, 16501-16514. [8] Collins, G. S., et al. (2002) *Icarus*, 157, 24-33. [9] Ivanov, B. A., DeNeim, D. and Neukum, G. (1997) *Int. J. Imp. Eng.* 20, 411-430. [10] Ivanov, B. A. and Deutsch, A. (1999) *Spec. Paper GSA* 339, 389-397. [11] Amsden, A.A., Ruppel, H.M., and Hirt, C.W., (1980) *LANL Report LA-8095, Los Alamos, NM*. [12] Johnson, G. R. and Holmquist, T.J. (1994) In: *High-Pressure Science and Technology – 1993, AIP Press, Woodbury NY*, 981-984. [13] Melosh, H. J., Ryan, E. V. and Asphaug, E. (1992) *JGR* 97 #E7, 14735-59.

Acknowledgements: This research was supported by NASA grant NAG5-11493.

MESOSCALE COMPUTATIONAL INVESTIGATION OF SHOCKED HETEROGENEOUS MATERIALS WITH APPLICATION TO LARGE IMPACT CRATERS. D. A. Crawford¹, O. S. Barnouin-Jha², and M. J. Cintala³, ¹Sandia National Laboratories, Albuquerque, NM, USA (dacrawf@sandia.gov), ²The Johns Hopkins University Applied Physics Laboratory, Laurel, MD USA, ³NASA Johnson Space Center, Houston, TX, USA.

Introduction: The propagation of shock waves through target materials is strongly influenced by the presence of small-scale structure, fractures, physical and chemical heterogeneities. Pre-existing fractures often create craters that appear square in outline (e.g. Meteor Crater) [1,2]. Reverberations behind the shock from the presence of physical heterogeneity have been proposed as a mechanism for transient weakening of target materials [3]. Pre-existing fractures can also affect melt generation [4].

In this study, we are attempting to bridge the gap in numerical modeling between the micro-scale and the continuum, the so-called meso-scale. To accomplish this, we are developing a methodology to be used in the shock physics hydrocode (CTH) [5] using Monte-Carlo-type methods to investigate the shock properties of heterogeneous materials. By comparing the results of numerical experiments at the micro-scale with experimental results [6] and by using statistical techniques to evaluate the performance of simple constitutive models, we hope to embed the effect of physical heterogeneity into the field variables (pressure, stress, density, velocity) allowing us to directly imprint the effects of micro-scale heterogeneity at the continuum level without incurring high computational cost.

Approach: To demonstrate our numerical approach, a two dimensional computation of a mixture of two fictitious materials was carried out using the adaptive mesh refinement capability [7] of CTH (see Figs. 1 and 2). Each material is described with a linear shock-particle velocity equation-of-state (EOS). A two-dimensional plane-strain approximation is used. A flyer plate of the higher impedance material impacts a target created by the mixture of the two materials. The mixture is created with a random distribution of 500 equal-sized 2 mm square grains of the high impedance material embedded within a matrix of the lower impedance material. The average volume fraction of the grains is 0.298 with mass fraction of 0.459. Impact velocities of 1, 2 and 4 km/s were used to generate six Hugoniot states in the materials (three in the projectile and three in the target).

We can treat this numerical experiment as if it was a true Hugoniot experiment. By measuring the shock and particle velocities through the materials, we can determine if the mixture of two linear shock-particle velocity materials will also behave as a linear shock-particle velocity material. Figure 3 shows the three Hugoniot points determined for the target material as

clearly falling on a linear relationship between the high impedance and low impedance materials. Furthermore, we see that these values very well match the additive mixture EOS of Grady [8], as shown in Fig. 4.

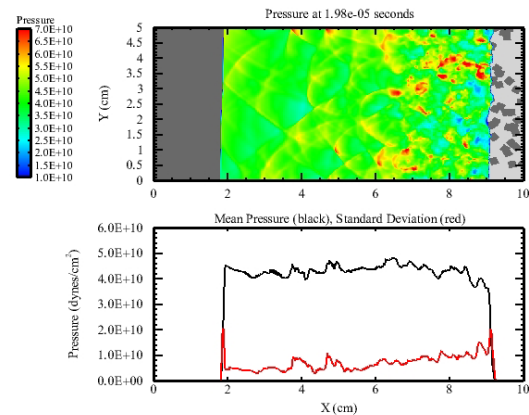


FIGURE 1. Two dimensional CTH simulation using adaptive mesh refinement of a high impedance plate of material striking a heterogeneous material consisting of a mixture of high impedance grains embedded in a low impedance matrix. The pressure field is shown in the upper plot. Mean pressure and its standard deviation are shown in the lower plot.

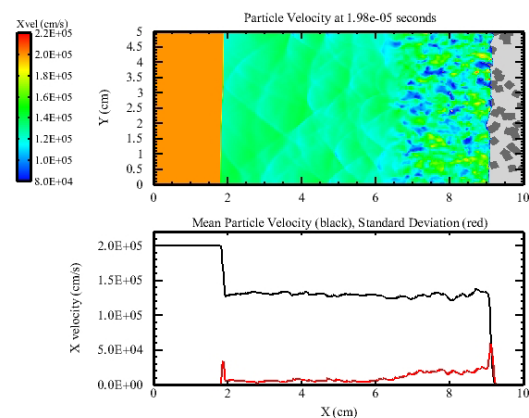


FIGURE 2. The same numerical experiment as Fig. 1 showing particle velocity instead of pressure. The particle velocity field is shown in the upper plot. Mean particle velocity and its standard deviation are shown in the lower plot.

Conclusions/Future Work: We are establishing a methodology using adaptive mesh refinement with Monte-Carlo techniques to study material heterogeneity showing that even simple material systems can ex-

hibit interesting properties when spatial heterogeneity added to the mix. We are adding new capabilities to CTH to automate generation of Monte Carlo runs and some of the analysis. We are beginning to look at means to add variance at continuum level based on Monte Carlo studies at the mesoscale and we are looking at more complex material models involving shear and fracture strength. We will report results from additional numerical experiments and comparison with impact experiments. We believe that this approach will provide insight into the link between heterogeneity at the micro and continuum scales with eventual application to advanced geological material models useful for understanding large crater formation.

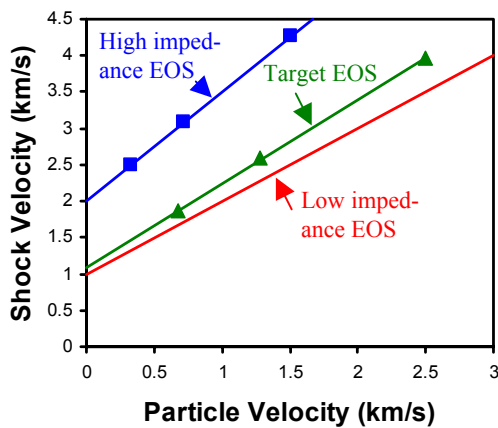


FIGURE 3. Plot of shock velocity vs. particle velocity from the numerical experiment shown in Figs. 1 and 2. The target EOS mixture also has a linear relationship falling between the low and high impedance materials.

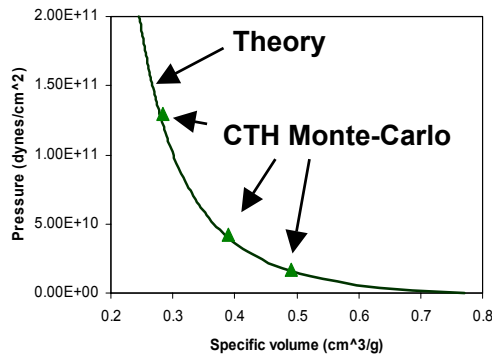


FIGURE 4. The Hugoniot for the three numerical experiments described in the text versus the additive mixture EOS theory of Grady [8].

References: [1] Fulmer, C.V. and W. A. Roberts, *Icarus* 2, 452-465, 1963. [2] Shoemaker, E.M., In *The Moon, meteorites and comets*, Univ. of Chicago Press, Chicago, 1963. [3] Melosh, H. J., *JGR* 84, 7513-7520 (1979). [4] Kieffer, S.W., *Jour. of Geophys. Res.*, 76, 5449-5473, 1971. [5] Barnouin-Jha, O.S., M.J. Cintala and D. A. Crawford (2002), *LPS XXXIII*, 1738-1739. [6] McGlaun, J.M., S.L. Thompson and M.G. Elrick (1990) *Int. J. Impact Eng.*, 10, 351-360. [7] Crawford, D. A., *et al.*, *New Models and Hydrocodes for Shock Wave Processes in Cond. Matter*, Edinburgh, U.K., May 19-24, 2002, (in press). [8] D. E. Grady, *Shock Compression and Release Properties of Metal-Ceramic Mixtures*, *Sandia National Laboratories Report, SAND93-2325J* (1993).

Acknowledgements: Sandia is a multi-program laboratory operated by Sandia Corporation, a Lockheed Martin Company, for the United States Department of Energy under Contract DE-AC04-94AL85000.

A MODEL OF EARLY CONDENSATE COMPOSITION IN IMPACTS. D. de Niem, *Institute of Space Sensor Technology and Planetary Exploration, German Aerospace Center, D-12489 Berlin, Germany, (detlef.deniem@dlr.de).*

Anomalies of the abundance of siderophile elements in high-temperature condensates are among the most important tracers of terrestrial impacts [1, 2]. Initial pressures and temperatures during terrestrial impact are sufficient to cause complete vaporization of most of the projectile and a comparable amount of target rocks [5, 6]. The gas phase mostly consists of a large number of molecular species (oxides and other compounds) while pure atomic gases are far less abundant. Original meteoritic abundances are not likely to be preserved in high-temperature condensates. In early condensates, the concentration of siderophile elements occurs preferentially in small metallic grains. These grains can form under pressures comparable to or slightly larger than the ambient atmospheric pressure (at altitudes up to several tens of kilometers) and temperatures exceeding 3000 K. Due to the rapid adiabatic expansion, condensate abundances tend to 'freeze out' when reaction rates drop. Previous calculations of chemical equilibria in impacts [3, 4] have been confined to lower temperatures and used a prescribed (P, T) path extracted from hydrocode calculations.

In this work, the simultaneous thermodynamic and compositional evolution of impact-created vapor is investigated numerically. The thermal evolution is treated consistently, using the actual abundances and thermodynamic properties of the mixture of gases and condensed material (which presently is too complex for hydrocode calculations). A previous derivation of the energy equation [7] is generalized to multiple species, incorporating the constraints of the overall elemental mass balance and dissociation equilibrium in the gas phase. These constraints, which also appear in the traditional approach of minimization of the total Gibbs potential [8], are more easily applied in the form of differential equations. The energy equation is solved simultaneously with certain equations for the evolution of gaseous and condensed-phase abundances. In particular, the differential equations for molecular abundances in the gas phase follow from chemical equilibrium, and some other equations describing the degree of condensation of each element are obtained either from phase equilibrium or by solving some model of kinetics of phase transitions. Liquids of variable composition are modelled as ideal solutions, and stoichiometric solids in coexistence with the gas phase are included, using thermochemical data in [8]. In a Lagrangean formulation, the only independent hydrodynamic variable is the local volume expansion rate, $\dot{\rho}/\rho$. The latter is approximated for a spherically symmetric model, using a semianalytical solution [7], similar to that of Zeldovich and Raizer [9]. This approach, being a large simplification as far as hydrodynamics is concerned, has the advantage of making less a compromise from the thermodynamic point of view. For an initial state of gas-phase chemical equilibrium, subsequent states maintain chemical equilibrium, if nucleation kinetics is excluded. In this case, the model is numerically less expensive than a global minimization of Gibb's potential. Furthermore,

it has the advantage of following the actual thermodynamic evolution, rather than using a prescribed (P, T) path.

Preliminary results are presented, showing trends for abundances of metallic grains to be expected as high-temperature condensates. It is pointed out, which type of information about formation temperatures during condensation can be obtained from abundances. Possible extensions of the model to include nucleation kinetics are described.

References

- [1] Kyte, F. T., Bostwick, J. A. 1994: *Magnesioferrite spinel in Cretaceous/Tertiary boundary sediments of the Pacific basin: Remnants of hot, early ejecta from the Chicxulub impact ? Earth and Planet. Sc. Lett.* 132, 113-127.
- [2] Bauluz, B., Peacor, D. R., Elliot, W. C. 2000: *Coexisting altered glass and Fe-Ni oxides at the Cretaceous-Tertiary boundary, Stevns Klint (Denmark): direct evidence of meteorite impact. Earth and Planet. Sc. Lett.* 182, 127-136.
- [3] Ebel, D. S., Grossmann, L. 1999: *Condensation in a model Chicxulub fireball. 30th Ann. Lunar and Planet. Sc. Conf., abstr. no 1906.*
- [4] Ebel, D. S., Grossmann, L. 2001: *Condensation from the plume of an oblique Chicxulub impact. Meteoritics and Planetary Science 26, supplement, A53.*
- [5] Melosh, H. J., Pierazzo, E. 1997: *Impact vapor plume expansion with realistic geometry and equation of state. 28th Ann. Lunar and Planet. Sc. Conf., p. 935.*
- [6] Pierazzo, E., Kring, D.A., Melosh, H. J. 1998: *Hydrocode Simulation of the Chicxulub impact event and the production of climatically active gases. J. Geophys. Res.* 103, 28607-28626.
- [7] de Niem, D. 2002: *Multiple stages of condensation in impact-produced vapor clouds, in Koeberl, C, and MacLeod, K. G., eds., Catastrophic Events and Mass Extinctions: Impacts and Beyond: Boulder, Colorado, Geol. Soc. Amer. Special Paper 356, 631-644*
- [8] Sharp, C. M., Huebner, W. F. 1990: *Molecular equilibrium with condensation. Astrophys. J. Suppl.* 72, 417-431.
- [9] Zeldovich, Ya. B. , Raizer, Yu. P.: *Physics of Shock Waves and High-Temperature Hydrodynamic Phenomena, Academic Press, New York, San Francisco, London, 1967.*

ON THE SHOCK BEHAVIOR OF ANHYDRITE AND CARBONATES – IS POST-SHOCK MELTING THE MOST IMPORTANT EFFECT? EXAMPLES FROM CHICXULUB. A. Deutsch¹, F. Langenhorst², U. Hornemann³, B. A. Ivanov⁴, ¹Univ. Münster, Inst. f. Planetologie, Wilhelm-Klemm-Str. 10, D-48149 Münster, Germany, <deutsch@uni-muenster.de>, ²Bayerisches Geoinstitut, D-95440 Bayreuth, Germany, <falko.langenhorst@uni-bayreuth.de>, ³Ernst-Mach-Institut, Am Klingelberg 1, D-79588 Efringen-Kirchen, Germany, <hornema@wiwei.emi.fhg.de>, ⁴Inst. f. Dynamics of Geospheres, RAS, Moscow, Russia 117939, <baivanov@online.ru>

Introduction: To address the shock behavior of sulfate and carbonates, we performed shock experiments [1], and studied impact melt rocks, impact melt breccias, and suevites from Chicxulub drill cores.

Observation: Textural features and clast population of these impactites vary strongly as function of the formation temperature T (Fig. 1). *Melt rocks* (tagamite) mostly lack sulfate and carbonate clasts. Obviously their absence reflects the extremely high formation temperature, which caused thermal dissociation of CaSO_4 and CaCO_3 fragments. *Melt breccias* contain Ca-rich pyroxene and plagioclase, seen as evidence for dissociation of CaSO_4 . Large CaSO_4 clasts display corroded margins and consist of equant-sized, defect-free crystals with 120° triple junctions, indicating incomplete dissociation and solid-state recrystallization. *Melt breccias* with a low T contain clasts displaying the original sedimentary texture as well as blebs interpreted as CaCO_3 that crystallized from melted sedimentary clasts (Fig. 2). In *suevites*, annealed anhydrite clasts are nearly absent. An important feature are the $<100 \mu\text{m}$ wide “degassing” veins of anhydrite + calcite + quartz, which cut the matrix of all lithologies.

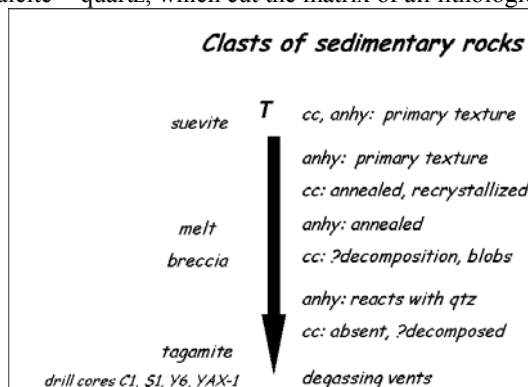


Fig. 1. Impact metamorphism (i.e., shock and post-shock annealing effects) of sedimentary clasts as function of formation temperature T . cc = calcite, anhy = anhydrite, qtz = quartz.

Interpretation: The combined results of observations on natural samples, from shock recovery experiments, and preliminary $\delta^{34}\text{S}$ values [2] establish the high stability of anhydrite under strong shock compression. Moreover they demonstrate that CaSO_4 does not decompose upon release from shock pressures, probably as high as 100 GPa. The construction of an adequate

EOS is required to better assess threshold pressure and related peak temperature, from which CaSO_4 would directly unload into fields of liquid and vapor (cf. [3] for the EOS of CaCO_3). Usually, devolatilization of minerals is considered as shock effect in a late stage of, or mainly after decompression, i.e., high post-shock temperatures are required. We propose that *the amplitude of post-shock temperatures is not the only driving force/major reason for devolatilization of sedimentary lithologies but also the formation temperature in the natural impact rock.*

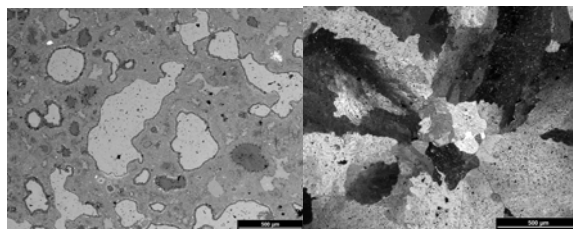


Fig. 2. Blebs of CaCO_3 mantled by a clay mineral, in a matrix of Ca-rich plagioclase whisker crystals and impact melt glass, altered to smectites (left). Feathery texture of the calcite indicates crystallization from a melted sedimentary clast under stress (right). YAX-1_835.77m; SEM.

Implications for the killing scenario in aftermath of the Chicxulub event: The observations provide solid evidence for melting and dissociation of evaporite and carbonates clasts in the hot impact melt layer, and massive release of CO_2 and SO_x . Timing, however, differs drastically from the classic idea of instant CO_2 and SO_x release in cratering. Devolatilization of sedimentary clasts in breccias may happen over a long time after the impact event. This “delayed” gas release, however, is unlikely to contribute to global effects, necessary to cause mass extinction.

References: [1] Langenhorst F. et al. (2002) in High-Pressure Shock Compression of Solids V - Shock Chemistry with Applications to Meteorite Impacts (eds. L. Davison et al.) Springer, 1-27. [2] Strauss H., Deutsch A. (2003) EUG-EGS-AGU-2003-Nice Session EAE03-A-04905. [3] Ivanov B.A., Deutsch A. (2002) PEPI 129, 131-143.

Acknowledgments: This work is supported by DFG grants DE 401/15-4, HO 1446/3-4, and LA 830/4-4, and the Humboldt-Stiftung (BAI). We are indebted to E. Lounejeva (UNAM) for fruitful discussions.

SYNTHESIS OF NANOCRYSTALLINE DIAMOND AND 6H DIAMOND POLYTYPE. N. Dubrovinskaia, L. Dubrovinsky, F. Langenhorst, Bayerisches Geoinstitut, University Bayreuth, D-95440 Bayreuth, Germany.

Natural elemental carbon occurs in its low-pressure polymorph graphite (2H space group $P6_3/mmc$ or 3R space group $R3m$) and the high-pressure polymorphs, cubic diamond (space group $Fd3m$) and hexagonal lonsdaleite (space group $P6_3/mmc$). Trace amounts of fullerenes were encountered in carbonaceous residues chemically extracted from carbonaceous meteorites and some terrestrial impact breccias [1,2]. Graphite, diamond and lonsdaleite occur in many meteorites as shock products, particularly in ureilites and iron meteorites, and in a variety of terrestrial impact rocks [3, 4]. The graphite-to-diamond and graphite-to-lonsdaleite phase transformations are reconstructive and require a change in the bonding type from sp^2 to sp^3 . Details of the transformation mechanisms and of the carbon phase diagram at high pressures and temperatures are however still not clear. To decipher the formation mechanisms and conditions of natural events (like meteoritic impacts), it is hence required to better understand the stable and metastable relations in the carbon system.

Here we report synthesis of a bulk sample of nanocrystalline cubic diamond and a new 6H diamond-like polytype with crystallite sizes of 8-12 nm. The sample was synthesized from fullerene C_{60} at 20(1) GPa and 2000(50) °C in a multi-anvil apparatus. Our findings indicate that the mechanism and products of transformations in the carbon phases depend strongly on the P-T-path and the structural state of the starting material.

References: [1] Heymann D., Chibante L. P. F., Brooks R. R., Wolbach W. S., Smally R. S. (1994) *Science*, 256, 545-548. [2] Becker L., Poreda R. J., Bada J. L. (1996) *Science*, 272, 249-252. [3] Masaitis V.L. (1998) *Meteoritics and Planetary Science*, 33, 349- 359. [4] Masaitis V.L., Shafranovsky G.I., Ezer-sky V.A., Reshetnyak N.B. (1990) *Meteoritika*, 49, 180-195.

PHASE RELATIONS IN TiO₂ AT ELEVATED PRESSURES AND TEMPERATURES. L. Dubrovinsky, N. Dubrovinskaia, Bayerisches Geoinstitut, University Bayreuth, D-95440 Bayreuth, Germany.

Titanium dioxide (TiO₂) occurs in nature as the accessory minerals rutile, anatase, and brookite. Rutile is the most abundant TiO₂ polymorph in nature and is an important minor constituent in natural rocks. It is isostructural with stishovite. Hence, its response to static and dynamic pressure is important for understanding phase transition mechanisms in SiO₂ and TiO₂ during subduction of crustal limbs to the Earth's mantle and during natural shock events. Recently the first natural occurrence of a shock-induced dense α -PbO₂-structured polymorph of TiO₂ was found in gneisses from the Ries crater in Germany.

The phase relations in TiO₂ system at elevated pressures and temperatures are not fully understood and it motivated us to conduct a series of experiments in laser- or electrically-heated diamond anvil cells (DACs). Anatase or rutile (99.99% TiO₂) was used as a starting material. At applied pressures of about 12 GPa or above, both rutile and anatase transform to the baddeleyite (MI, *P2₁/c*) phase. On further compression, reflections due to the MI phase could be followed to over 60 GPa. At pressures above about 45 GPa, however, the quality of the diffraction pattern decreased drastically and at about 60 GPa, the material became translucent. We observed that at pressures above 50 GPa, TiO₂ absorbs Nd:YAG laser radiation and the laser-heated areas of the sample became black. After heating at 1600-1800 K by laser for 40 minutes at pressures between 60 and 65 GPa, the material transformed to a new phase. All X-ray reflections of the new phase could be indexed in an orthorhombic cotunnite-type cell. Transformations observed by X-ray diffraction were confirmed by Raman spectroscopy. Although *in situ* high pressure and temperature Raman spectroscopy in DACs does not provide direct structural information, this method is much faster and experimentally easier for realisation than X-ray powder diffraction. Raman signals from all titania phases are strong and clearly distinguishable and we used Raman spectroscopy to follow some phase relations in TiO₂ at high-P,T conditions. Particularly, we found that slope of phase boundary between α -PbO₂-type TiO₂ and MI phase (77(3) K/GPa) is significantly lower than that earlier reported by Tang and Endo (1993) (188 K/GPa).

Our combined theoretical and experimental investigations have led to the discovery of new polymorphs of titanium dioxide, where titanium is seven-coordinated to oxygen in the orthorhombic OI (*Pbca*) structure and nine-coordinated in cotunnite-type phase (OII, space group *Pnma*). We demonstrate that the group IVa dioxides (TiO₂, ZrO₂, HfO₂) on compression at ambient temperature all follow the common path: rutile \rightarrow α -PbO₂-type \rightarrow baddeleyite-type (MI) \rightarrow orthorhombic OI (*Pbca*) structure \rightarrow cotunnite-type (OII). Bulk modulus of OI and OII phases are high (318 GPa and 431 GPa) respectively, and the hardness of cryogenically quenched OII phase is 36-38 GPa.